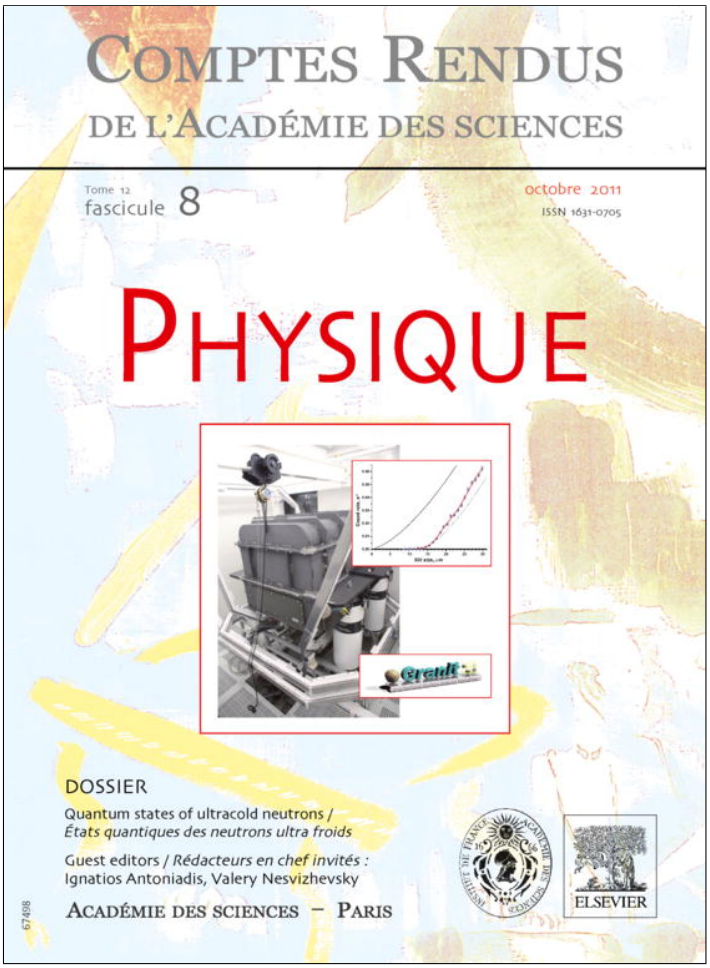

C. R. Physique 12 (2011) 729–754

Contents lists available at ScienceDirect

Comptes Rendus Physique

www.sciencedirect.com

Ultra cold neutron quantum states / États quantiques des neutrons ultra froids

New methodical developments for GRANIT

Nouveaux développements méthodologiques pour GRANIT

S. Baessler [a,b], A.M. Gagarski [c], E.V. Lychagin [d], A. Mietke [e], A.Yu. Muzychka [d], V.V. Nesvizhevsky [f,*], G. Pignol [g], A.V. Strelkov [d], B.P. Toperverg [c,h], K. Zhernenkov [h]

[a] *University of Virginia, Charlottesville, VA-22904, USA*
[b] *Oak Ridge Nat. Lab., Oak Ridge, TN-37831, USA*
[c] *PNPI, Orlova Roscha, Gatchina, RU-188300, Russia*
[d] *JINR, 6 Joliot-Curie, Dubna, RU-141980, Russia*
[e] *Faculty of Science, Department of Phys., Technical University, Dresden, G-01062, Germany*
[f] *ILL, 6 rue Jules Horowitz, Grenoble, F-38042, France*
[g] *LPSC/IN2P3-UJF-INPG, 53 rue des Martyrs, Grenoble, F-38026, France*
[h] *Ruhr Univ. Bochum, 150 Universitatstrasse, Bochum, G-44780, Germany*

ARTICLE INFO

Article history:
Received 16 January 2011
Acepted after revision 29 April 2011
Available online 3 August 2011

Keywords:
Ultra cold neutrons
Quantum mechanics
Gravitation
High-resolution spectroscopy
Nanoparticles
Neutron detectors

Mots-clés :
Neutrons ultra froids
Mécanique quantique
Gravitation
Spectroscopie à haute résolution
Nanoparticules
Détecteurs de neutrons

ABSTRACT

New methodical developments for the GRANIT spectrometer address further improvements of the critical parameters of this experimental installation, as well as its applications to new fields of research. Keeping in mind an extremely small fraction of ultra cold neutrons (UCN) that could be bound in gravitational quantum states, we look for methods to increase statistics due to: developing UCN sources with maximum phase-space density, counting simultaneously a large fraction of neutrons using position-sensitive detectors, and decreasing detector backgrounds. Also we explore an eventual application of the GRANIT spectrometer beyond the scope of its initial goals, for instance, for reflectometry with UCN.

RÉSUMÉ

De nouveaux développements méthodologiques relatifs au spectromètre GRANIT concernent l'amélioration des paramètres critiques de cette installation expérimentale, ainsi que des applications à de nouveaux domaines de recherche. Compte tenu du nombre extrêmement faible de neutrons ultra froids (UCN) qui pourraient être liés dans les états quantiques gravitationnels, nous recherchons des moyens d'améliorer la statistique afin de développer des sources UCN dont la densité est maximale dans l'espace des phases, de compter simultanément une large fraction de neutrons en utilisant des détecteurs sensibles à la position, et de diminuer le bruit de fond des détecteurs. En outre, nous étudions une application éventuelle du spectromètre GRANIT au-delà de ses objectifs initiaux, par exemple pour la réflectométrie avec des UCN.

* Corresponding author.
E-mail address: nesvizhevsky@ill.eu (V.V. Nesvizhevsky).

1631-0705/$ – see front matter
doi:10.1016/j.crhy.2011.04.014

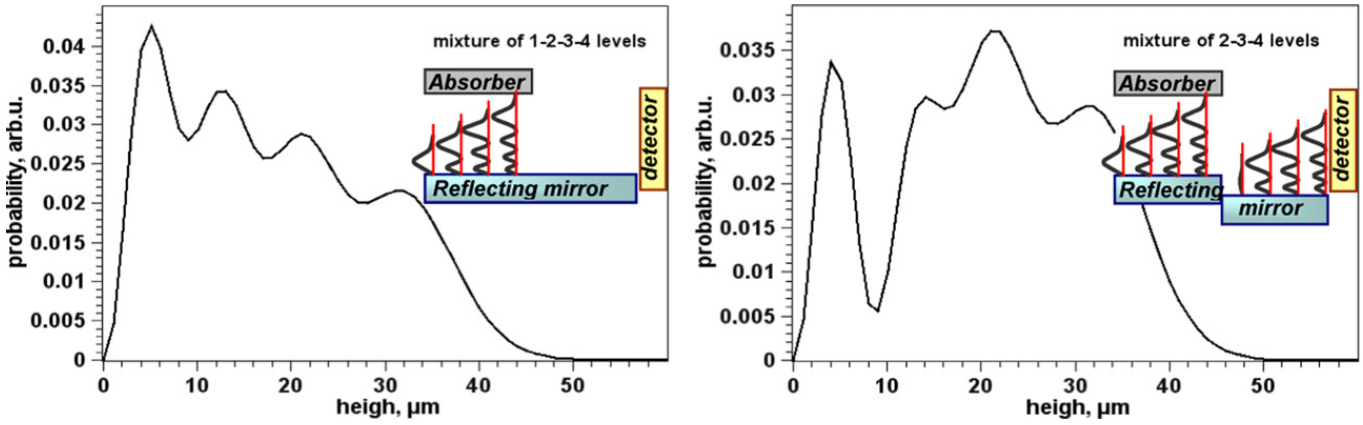

Fig. 1. The height distribution of UCNs above a mirror. Left panel – 4 lowest quantum states, right panel – 2–4th quantum states. Principle schemes to form the corresponding mixtures of states are shown in the inserts.

Fig. 1. Distribution des hauteurs des UCN au-dessus du miroir. Figure de gauche : les 4 premiers états quantiques ; figure de droite : états quantiques 2–4. Le principe de formation des combinaisons d'états est indiqué dans les inserts.

1. Introduction

New methodical developments for the GRANIT spectrometer [1–3] address eventual further improvements of some critical parameters of this experimental installation, as well as its application to new fields of research.

Keeping in mind an extremely small fraction of ultra cold neutrons (UCN) [4–6] that could be bound in gravitational quantum states [7–11] we look for methods to increase statistics due to developing UCN sources with maximum phase-space density [12–14] and counting simultaneously a large fraction of neutrons using position-sensitive detectors [15,16]. On the other hand, we have to reduce backgrounds in our UCN detectors [15]. Significant efforts are devoted to develop neutron optics [17,18] for GRANIT, and spectrum shaping devices [19–23].

Also we explore an eventual application of the GRANIT spectrometer beyond the scope of its initial goals, such as, for instance, constraining short-range interactions [24–26] using gravitational and centrifugal [27–30] quantum states of neutrons: it might be used, for instance, for prototyping experiments with gravitational quantum states of anti-hydrogen [31], or as a UCN general-purpose reflectometer. The physics to be studied as well as some methodical approaches to carry out such measurements are given.

Section 2 presents state-of-the-art concerning nuclear-track position-sensitive detectors for UCNs with 1 μm resolution, which were developed for studies of/with neutron gravitational quantum states; they will be widely used in the GRANIT spectrometer. Information on parameters of quantum states that could be extracted from measurements of neutron wave-functions is discussed in Section 3. Section 4 describes state-of-the-art in low-background counters of slow and ultra cold neutrons. Position-sensitive UCN detectors for measurements of gravitational levels are overviewed briefly in Section 5; in particular, real-time position-sensitive detection and spectroscopy of UCN with micrometric resolution are described in Section 6. An introduction to elastic and inelastic neutron scattering at grazing incidence, with emphasis on advantages of long wavelength, is given in Section 7. AC magnetometry with polarized neutron scattering: motivations, feasibility and applications, is presented in Section 8. Collimators for shaping neutron spectra for studies of gravitational quantum states and for UCN reflectometry are discussed in Section 9. Study of reflectors for GRANIT UCN source, as well as a new concept of "virtual" cold neutron source for UCN production in super-thermal helium are described in Section 10. Section 11 presents recent developments on nanoparticle reflectors for cold and very cold neutrons. Developments on impurity quantum sols in superfluid He-II are mentioned in Section 12.

2. Nuclear-track position-sensitive detectors for UCNs with 1 μm resolution (Alexei Gagarski)

One goal for the GRANIT spectrometer is to study wave functions of UCN in quantum states above a mirror. These distributions are defined by a superposition of Airy functions [15]; an example for four equally populated lowest levels, interference terms ignored, is presented in Fig. 1 (left).

One could get better pronounced variation of UCN density above a mirror by suppressing population of neutrons in the ground state by letting them to fall off a step on the mirror [32]. UCNs in the lowest state in front of the step would be spread, after dropping between a few quantum states, in such a way that population of the lowest state is suppressed on right from the step (Fig. 1 (right)). The idea is to place a position-sensitive detector to the mirror edge and measure the UCN density distribution. The main requirements for such a detector are the following:

a) Position resolution in the vertical direction is $\sim$ 2–3 μm or better, since expected structures in the UCNs spatial distribution are modulated on a characteristic length scale of $\sim$ 10 μm;
b) Reasonable efficiency of at least $>$ 10%, since the flux of neutrons in quantum states is low;

c) Required sensitive area is ~ 100 μm $\times$ 30 cm;
d) Detector internal background should be very low.

Probably detectors of only one type meet these requirements: solid-state nuclear-track detectors (SSNTD) measuring tracks of ionizing particles. Neutrons can be converted to charged particles via some nuclear reaction; a proper neutron capturing material should be deposited on an SSNTD surface for this purpose. Three practically feasible reactions – $^{6}\mathrm{Li}(n,{}^{3}\mathrm{H})^{4}\mathrm{He}$, $^{10}\mathrm{B}(n,{}^{4}\mathrm{He})^{7}\mathrm{Li}$, and $^{235}\mathrm{U}(n,\text{fission})$ – will be compared below.

Basic principles of SSNTDs are simple. Heavy charged particles ionize extensively the detector material. This ionization triggers some chemical processes. Thus a zone around the particle path becomes enriched with free radicals and other chemical species. The damaged zone diameter is of the order of 100 Å, and the zone is called a latent track. Chemical properties of material in the latent tracks are different from those in the bulk. When we place the detector material in some aggressive chemicals, etching of the damaged core will go faster than that in the bulk. The "track" could be enlarged by chemical etching to the size visible in an optical microscope. Such nuclear tracks could be recorded in many natural materials (apatite, mica, olivine, etc.), also in artificial ones (polymers and glasses). Materials with long complex molecules, especially polymers, are most sensitive to damage.

The history of SSNTDs is more than half a century long. Since then, there has been a tremendous growth in this field of science. There is a wide range of applications of SSNTDs in basic and applied research: nuclear physics, cosmic ray physics, radon monitoring, neutron dosimetry, heavy ion radiography, medicine and biology. A disadvantage of SSNTDs is that these are off-line detectors. It means that the data can be read only after completing exposition of a detector to neutrons, then after time-consuming chemical procedures. This topic was reviewed in several books, for example in [33].

The etching process is analogous to the Huygen's principle of wave propagation: each point in the material, opened to etching, is a center of etching sphere with a radius $R = V_b t$, where t is the etching time, and V_b is the etching rate of non-damaged material in the bulk. The etching progresses with the rate V_t only along the latent track channel. The development of the track shape during chemical etching is governed by the so-called reduced etch rate: $P = V_t/V_b$, or sensitivity. Etched tracks at the first stage of the processing look like cones with the opening angle $\delta = \arcsin(1/P)$ (in the approximation of constant P over the track length), and at the very last stages they become sphere segments. Evidently, particles injected at an angle $\theta < \arcsin(1/P)$ to the detector surface cannot be measured.

Both V_b and V_t, as for every chemical process, depend on the concentration of etching reactive and the temperature. However, for a specific detector material, the reduced etch rate P is a function of the ionization damage only. P is usually approximated in terms of the so-called "restricted energy loss" of the ionizing particle (REL) by some increasing function of a type:

$$P = \sum_i \alpha_i (\mathrm{REL})^{b_i} \tag{1}$$

where α_i, β_i are the fitting parameters attributed to every material.

REL is a fraction of the electronic energy loss of a particle in a material, which leads to producing of δ-electrons with the energies lower than some critical value $E_{\max}$ (typically equal to 200–500 eV for plastic materials). The δ-electrons with $E > E_{\max}$ are considered to go far away from the trajectory thus not participating in the formation of the critical ionization for the latent track formation. The REL is a function of a type of projectile and its velocity. It can be estimated using the Bethe and Bloch formula, within some range of ion velocities, or by special calculations based on the experimental data on energy loses for ions in materials; computer codes are available for this purpose [34].

The most commonly used nowadays material for SSNTDs is a polymer Polyallyl diglycol carbonate. It provides the best sensitivity (P) in a wide range of REL. It is available commercially as CR-39, see for example [35]. It is a clear colorless rigid plastic graded specially for SSNTD applications. Sodium or Potassium alkalis are generally used for etching tracks in CR-39. The sensitivity of CR-39 is well calibrated in terms of REL for a wide range of ions, from relativistic to low energetic ones, see for example Refs. [36,37].

Our detector looks very simple. It is a rectangular sheet of CR-39 with the thickness of 1.5 mm with a UCNs converter deposited directly on its surface. A scheme of neutron detection using SSNTD is shown in Fig. 2.

It is important to note that due to the fact that charged particles are emitted isotropically from the interaction point, there is a shift between the track entrance to the plastic (2, Fig. 2) and the actual points of neutron capture (1, Fig. 2):

$$\Delta = (h + d)/\operatorname{tg}(\theta) \tag{2}$$

where h is the converter thickness, d is the thickness of a layer removed from surface during etching, and θ is the angle of incidence of the charged particle. Δ (we call it "walk") is one of the main contributions to the spatial resolution. The minimum extent of etching (d) is defined by the requirement to make tracks visible in an optical microscope – for this purpose, the entrance track diameter D and the etched (visible) track length l should be equal to at least ~ 0.5–1 μm. Both D and l, as follows from the simple etching model mentioned above, are related to the surface etching d:

$$D = 2d(P-1)\tan\bigl(\arcsin(1/P)\bigr), \qquad l = d\bigl(P - 1/\sin(\theta)\bigr) \tag{3}$$

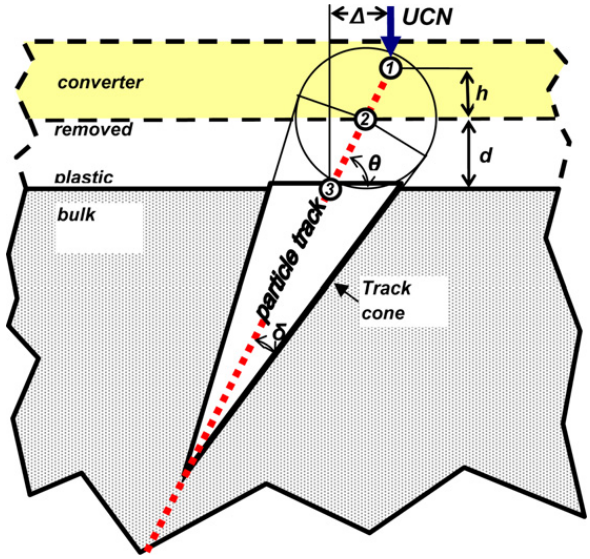

Fig. 2. Detection of UCNs in SSNTD. 1 – capture point, 2 – beginning of the latent track in plastic, 3 – center of the track entrance after etching.

Fig. 2. Détection des UCN dans le SSNTD. 1 : le point de capture ; 2 : début de la trace latente dans le plastique ; 3 : centre de la trace après décapage.

Table 1

Reaction	$n + {}^{6}\mathrm{Li} \rightarrow {}^{4}\mathrm{He} + {}^{3}\mathrm{H}$		$n + {}^{10}\mathrm{B} \rightarrow {}^{4}\mathrm{He} + {}^{7}\mathrm{Li}$		$n + {}^{235}\mathrm{U} \rightarrow$ fission
Compound	LiF		B (atomic)		UF_4
Enrichment	80%		80%		99.99%
Secondary ions	^{4}He (2.05 MeV)	^{3}H (2.73 MeV)	^{4}He (1.47 MeV)	^{7}Li (0.84 MeV)	Two fission fragments with energy ∼ 90 MeV
Range in CR39	8.9 μm	53 μm	6.5 μm	3.3 μm	∼ 15–20 μm
$P = V_t/V_b$	∼ 3	∼ 1.2	∼ 3	∼ 5	∼ 20
Track sizes					
Length (l)	1 μm	0.1 μm	1.1 μm	2 μm	10 μm
Input diameter (D)	0.7 μm	0.25 μm	0.8 μm	0.8 μm	1 μm
Efficiency					
Neutron capture	69%		100%		17%
Total	12%		43%		15%
V_{critical}	4.6 m/s		2.9 m/s		4.6 m/s

Thus $D \approx 2d$ and $l \gg d$ for $P \rightarrow \infty$ (highly ionizing particles) and $D = 1.15d$, $l < d$ for $P = 2$ (low ionization). As one can see, the minimum etching we need to provide in order to make the tracks optically visible, is $d \sim 0.5$ μm even for highly ionizing particles. The thickness h is determined by the converter material capture cross section and the required detector efficiency.

The optimization of the SSNTD position sensitivity for neutron detection is thus a problem of proper choice of the converter material, its thickness and the extent of etching. “Proper” etching procedure should provide tracks well visible optically, but keep the surface “walk” within reasonable range for good spatial resolution.

The plastic sensitivity P for conversion ions is the most important parameter, since it defines visibility of a track and, hence, the spatial resolution. It is also crucial for backgrounds – badly visible tracks can be easily misidentified with defects of the plastic surface. On the other hand, the P value limits efficiency, as only the ions entering the plastic at the angles θ steeper than $\arcsin(1/P)$ can be measured. There could be a further decrease in the actual efficiency because of an eventual optical cutoff in the reading procedure. Another converter parameter, which needs to be balanced against the detector efficiency in an actual experiment, is a critical velocity (neutron optical potential) of the converter, since a fraction of the UCN spectrum lower than some critical value would not enter to the converter bulk.

In Table 1, three converter materials, available and depositable on CR39 plastic, are compared. The isotopic enrichment of the material was assumed to be equal 80% for ^{10}B and ^{6}Li, and 99.99% for ^{235}U; such enrichments are available. The data in Table 1 are evaluated for neutrons with the velocity 5 m/s, for the convertor layer thickness 0.5 μm, and for the bulk etching $d = 0.5$ μm. The track length and the input diameter in Table 1 are calculated for a track directed perpendicular to the detector surfaces. In order to estimate the total efficiency using a Monte Carlo simulation, we counted only the tracks with the depth and the small axis of the entrance ellipse greater than 0.5 μm.

As follows from Table 1, a converter made of ^{235}U has a great advantage in visibility of the tracks; however it can provide efficiency of only ∼ 10–15% for an acceptable layer thickness. A ^{10}B converter can provide higher efficiency ∼ 40%, but not so well pronounced tracks as those for ^{235}U (for acceptable etching $d = 0.5$ μm); note that it provides the lowest critical velocity among the considered materials. Concerning a ^{6}Li converter: only tracks resulting from ^{4}He can be measured since

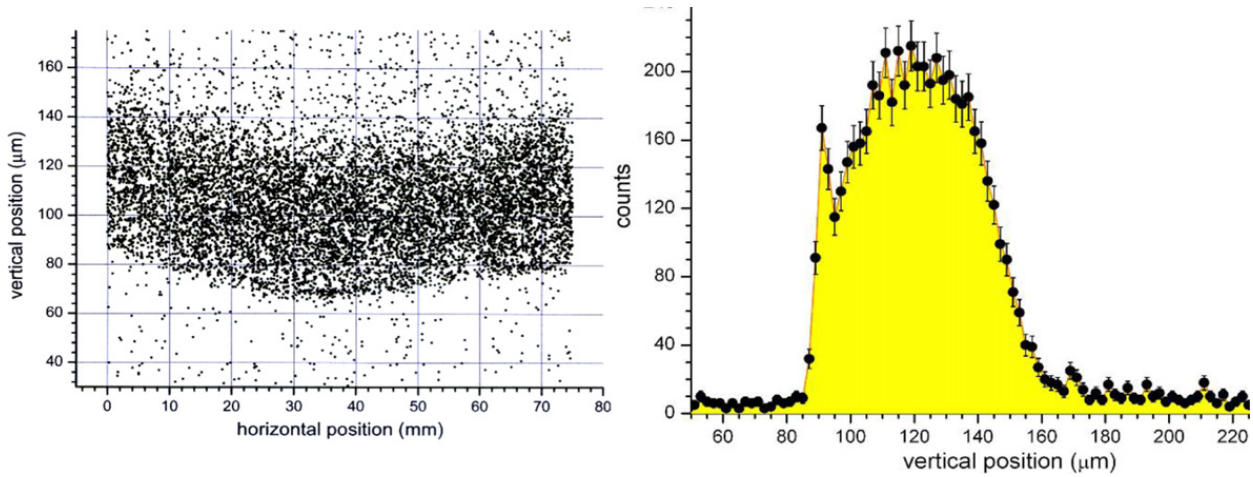

Fig. 3. Track distribution in a CR39 detector with a ^{235}U converter. Left panel – raw track coordinate distribution, right panel – vertical track distribution after applying correction for the shape deformation.

Fig. 3. Distribution des traces dans un détecteur CR39 avec un convertisseur ^{235}U. Figure de gauche : distribution des coordonnées brute ; figure de droite : distribution verticale des traces après correction de la déformation.

the sensitivity for ^{3}H (2.73 MeV) ions is very low, that is why it can provide only $\sim 12\%$ efficiency. On the other hand, from practical point of view, a ^{6}LiF converter is most easily available. In principle, all 3 converters meet our requirements.

It is important to note that the internal background in SSNTDs is determined by the number of defects in the plastic surface looking like tracks. Of course, it depends on the ionizing particle to be measured and on the regime of etching. With proper detector handling, it is much lower than our acceptable values. Usually reported values of the defects density are $< 10^2$ cm^{-2}, while we expect to have $> 10^4$ cm^{-2} of useful events in one exposition in the GRANIT experiments. External backgrounds are defined by external neutrons of various energies, not related to the signal of interest.

There are several practical problems, which should be solved to realize ideal calculated detector parameters:

a) Coating of a plastic with converter material should provide high adhesion and homogeneity. So far we use vacuum evaporation of a converter material. A thin sub-layer of aluminum $\sim$ 100–200 Å does not increase the thickness significantly, but provides high adhesion of the main layer.
b) Mechanical deformations of the detector between its exposition and reading out. A plastic plate is usually bended during etching by up to a few tens microns. Pre-etching of the material before evaporation helps. If statistics is high enough, one could correct the data by, for example, estimating some well-defined coordinate parameter of the measured neutron distribution (for instance, the mean value or the low edge position) for individual vertical slices over the detector length; then one could approximate this parameter by a polynomial function, which can be used to correct raw coordinate data for each track. It is also possible to apply a well-defined reference structure for the detector shape correction. It might be provided, for instance, by an additional irradiation of the detector with fully opened slit (high statistics); the detector being placed lower by ~ 100 μm than in the main measurement. By doing so, we will get an image of the mirror edge with high statistics as a reference, and a main image with only a few quantum levels thus lower statistics.
c) There is a known problem of vacuum degradation of the detector sensitivity. For the latent track formation, the plastic should contain some dissolved oxygen to "fix" the free radicals. Practically, the time constant of the oxygen outgassing is ~ 10 hours. So we should avoid long exposition of the detector in vacuum, or even perform measurements in oxygen atmosphere (~ 100 mb) which is not critical for UCNs in the flow-through measuring mode.
d) The coordinate-reading procedure should be precise and not very time-consuming. It is a main problem so far. With proper automatic image analysis, one could even correct for the "walk" of coordinate from the track geometry. If we can correct the track position for the "walk", the thickness of the removed layer would not be so critical anymore thus we could decrease background by longer etching, which makes track better distinguished from the background defects.

One can see in Fig. 3 the results of our first experiments with position-sensitive UCN detector based on CR-39 with a ^{235}U converter. The vertical density distribution of UCN passing the split between mirror and absorber was measured. The population of first quantum state was suppressed using 13.5 μm negative step on the mirrors. The detector after irradiation and etching was scanned in an optical microscope, and the data were recorded as a few hundred photos of approximately 70 mm of the horizontal image line. The detector's bending after etching was about 20 μm (see Fig. 3 (left)) and it was corrected by applying second order polynomial correction. To obtain the polynomial coefficients, the low edges of the distributions in individual 5 mm vertical slices were approximated by the second-order polynomial function. The vertical distribution of the track positions after correcting for the shape deformation is shown in Fig. 3 (right). One can notice the expected structure in the UCNs height distribution. A theoretical analysis of the data is presented in Section 3.

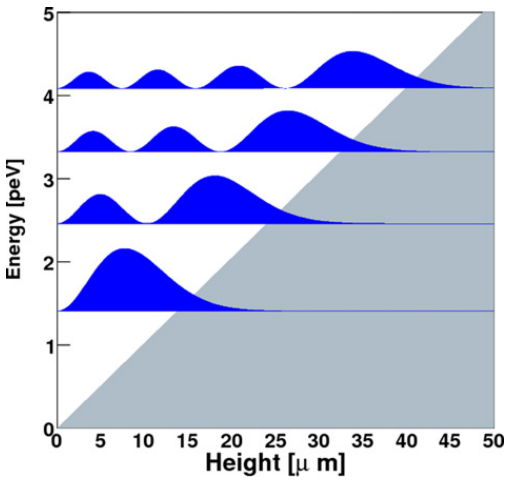

Fig. 4. Probability density functions for the four first gravitational quantum states. The four functions are translated vertically according to the energy of the state.

Fig. 4. Fonctions de densité de probabilité pour les quatre premiers états quantiques. Les graphes sont translates verticalement selon l'énergie de l'état quantique.

Nowadays, online detectors of any type cannot provide all required parameters for the GRANIT experiment, while SSNTDs made of CR-39 with ^{235}U (tetra fluoride) or ^{10}B converter deposited on its surface can meet the challenging requirements.

3. Measurements of neutron wave functions in quantum states (Guillaume Pignol)

A remarkable feature of quantum states of neutrons bouncing above a perfect mirror in the Earth's gravitational field is the large spatial extension of the wave functions. Indeed, the characteristic size of this quantum system is, from usual quantum theory (see, e.g. [15]):

$$z_0 = \left(\frac{\hbar^2}{2m^2 g}\right)^{1/3} = 5.87\ \mu\text{m} \tag{4}$$

The probability density for the discrete quantum states $P_n(z) = (\Psi_n(z))^2$ are squared Airy functions of the argument z/z_0, shown in Fig. 4. Such a macroscopic spatial extension allows measuring directly features of the wave functions using a position-sensitive neutron detector. This technique is described in Section 2. Here we present a statistical analysis of an experiment performed at PF2, ILL in 2005. This analysis is detailed in [38], it is based on the unpublished work of I. Ferrier-Barbut. For the experiment itself, credit has to be given to the authors of Ref. [9], as well as C. Krantz, L. Lucovac, J. Schrauven and S. Nahrwold.

The goal of the experiment was to observe the node of the second quantum state at 10 μm above the mirror's surface that the Schrödinger theory predicts, as evident in Fig. 4. In this flow-through experiment the quantum states were prepared by means of a horizontal mirror and a scatterer above, populating the first few quantum states. Details of the experimental apparatus can be found in [9]. In order to observe more clearly the node of the second quantum state, the population of the first quantum state has to be suppressed. The presence of higher excited states is not that much a problem for their probability density at 10 μm is reduced. An efficient suppression of the first quantum state population was done using a step [15]: neutrons are passing from a first horizontal mirror to a second one 13.5 μm lower. This gives enough gravitational energy to prevent populating the first quantum state after the step. Then the neutrons are detected with the position sensitive detector at the end of the second horizontal mirror.

The histogram of the 12 850 neutron counts on the detector is shown in Fig. 5. The exact height of the mirror h_0 is unknown at the micron level; it has to be adjusted on the data. But it is already clear from the figure that a node is present at a height of about 10 μm above the mirror's surface.

A general fitting procedure was applied to the data. The fitting function was parameterized as follows:

$$F(\beta_n, Bg, h_0, \sigma, z_0)(z) = \sum_{n=1}^{13} \beta_n P_n(\sigma, z_0)(z - h_0) + Bg \tag{5}$$

This contains 17 free parameters in total: β_n, $n - 1, \ldots, 13$, are the populations of the 13 first quantum states, Bg is a detector background count, h_0 is the offset height of the detector relative to the mirror, σ is the spatial resolution of the detector. Finally, the fundamental height z_0 was considered as a parameter to be adjusted. Adjusting a physical parameter is the simplest way to judge on the agreement between theory and measurement. The function $P_n(\sigma, z_0)(z)$ is the squared Airy wave function of the state n, with z_0 as a parameter, convoluted with a detector resolution σ, assumed to be Gaussian

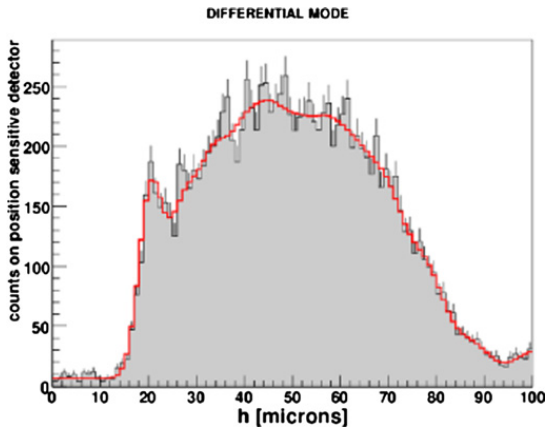

Fig. 5. Histogram of the neutron counts in the nuclear track detector. The line is the fit described in the text.

Fig. 5. Histogramme des hauteurs de neutrons dans le détecteur de traces nucléaires. La ligne représente l'ajustement discuté dans le texte.

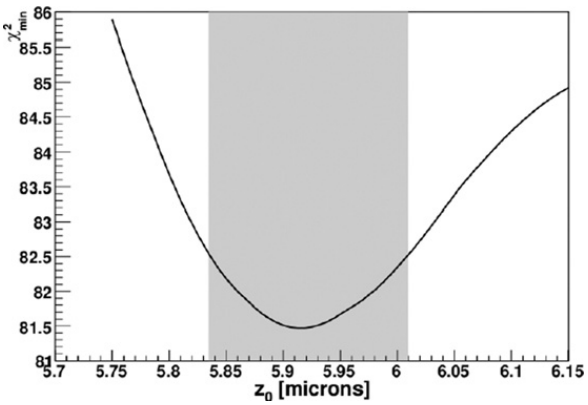

Fig. 6. Fit of the parameter z_0.

Fig. 6. Ajustement du paramètre z_0.

for convenience. Let us mention that this parameterization assumes that the neutrons populate the discrete quantum states incoherently, that is, interference terms of the form $\Psi_n(z)\Psi_m(z)$ for all $n \neq m$, were disregarded. However, these terms are expected to average to zero due to the horizontal velocity spread of the neutrons. A systematic uncertainty associated with the interference terms is yet to be estimated.

With so many parameters in the fit, special attention was paid to optimize and control the χ^2 minimization method. A dedicated program was written, taking advantage of the fact that parameters describing the populations and the background are linear parameters. Fixing the remaining three parameters z_0, σ and h_0, there is a single minimum for the χ^2 depending on the linear parameters which can be computed analytically. The procedure was repeated, scanning the nonlinear parameters z_0, σ and h_0 and it was checked that the χ^2 function eventually had a single minimum.

The line in Fig. 5 is the best fit (minimum $\chi^2 = 81.5/83$) to the data. The fitted detector's resolution is $\sigma = 2.05$ µm, in agreement with a first experimental check [2]. The fitted populations β_n show deviations with expectations. The data is consistent with non-zero populations of states up to number 9, whereas we expect a negligible population of the states higher than number 5 from a simple model of population after the step. This discrepancy was considered as an indication that random transitions populating excited states occurred in the way from the step to the detector, perhaps induced by mechanical vibrations of the mirror. However, this conclusion depends on the scatterer model. A more sophisticated treatment of the scatterer can reproduce theoretically the population of the states, except for the ground state [39].

In any case the fitting procedure does not require knowledge a priori of the population of the quantum states before the detector as they are considered as free parameters. The fit of the parameter z_0 is presented in Fig. 6, where for each fixed value of z_0 the minimum χ^2 with respect to the other 12 free parameters is given. This results in the fitted value $z_0 = 5.9 \pm 0.1$ µm. The whole fitting procedure has been applied for different number of populated quantum states taken into account in the analysis, to the real data as well as to fake data generated by Monte Carlo. After that the measured value has been reevaluated to:

$$z_0 = 5.9 \pm 0.2\ \mu\text{m} \tag{6}$$

in agreement with the expected value (4) with a relative accuracy of 3%. The result (6) is only the statistical analysis of the data. An estimate of diverse systematic effects has yet to be done. But already we can conclude that the method is successful in extracting information about the spatial structure of the gravitational quantum states of neutrons.

4. Low-background counters of slow and ultra cold neutrons (general principles and special aspects, Alexander Strelkov and Kirill Zhernenkov)

High detection efficiency and low internal background are the key characteristics of any radiation detector. They are of particular importance for UCN detectors for the experiments measuring quantum states of neutrons in the Earth's gravitational field in the GRANIT spectrometer (2), because the estimated flux of UCN in quantum states might be as low as 10^{-3}–10^{-2} s^{-1}. The present work describes general principles of operation of gaseous neutron detectors as well as special aspects of the neutron detector built for the GRANIT spectrometer.

In principle, a neutron of sufficiently high energy could ionize atoms directly due to its magnetic properties. However, its ionizing power is lower than that of, say, a proton by a factor of $\sim 10^6$. Therefore one first converts a neutron to ionizing particles (protons, α-particles, fission products, electrons, etc.), using reactions of neutrons with nuclei, in order to provide efficient neutron detection; then these ionizing particles are detected in a usual way.

There are neutron detectors of various kinds; however, we will focus on gaseous proportional counters [40] of slow neutrons, as the efficiency of these detectors for neutrons is high and the internal background is low. A scintillation detector with ^{6}Li + ZnS converter was used in the experiment on the very first observation of UCN; in nearly all following experiments UCN were detected using gaseous proportional counters with ^{3}He converters. Gaseous detectors with ^{3}He converter are relatively simple compared to scintillation detectors; they provide high efficiency, close to unity, and low sensitivity to γ-quanta.

A general scheme of a UCN detector with ^{3}He converter is the following:

UCN pass through a thin entrance window (usually made of an aluminum foil with a thickness of 50–100 μm), enter into a detector chamber filled in with mixture of gases including 5–10 mbar of ^{3}He. So small quantity of ^{3}He (the linear size of a detector along UCN beam direction is ~ 4 cm) is large enough for the total absorption of UCN, as the UCN absorption cross-section is proportional to the reversal neutron velocity $1/v$ thus it increases sharply for UCN, by a factor of 400–500, compared to that for thermal neutrons: $\sim 3400b$. Capture of UCN in ^{3}He in gaseous mixture: $n + {}^3\mathrm{He} \rightarrow p + T + 0.764$ MeV results in the emission of a proton p and a triton T with the energies 0.573 and 0.191 MeV respectively. These emitted charged particles produce ionizations tracks in the detector gas. If voltage of up to ~ 1 kV is applied to the detector anode, a thin wire with a diameter of 20–100 μm installed in the middle of the detector chamber, electrons and ions from the ionization track move to the respective electrodes thus providing an electrical signal in the electrodes. In this case, the detector is operated in the mode of an ionization chamber. If the detector would be filled in with ^{3}He with a pressure of ~ 5–10 mbar only, the ionization track length would be larger than the detector gas chamber size. If, however, Ar with the pressure of ~ 1000 mbar is added to gas mixture, the length of two tracks ($T + p$) is a few times smaller than the detector gas chamber size. So such detector provides electrical signals of equal amplitude; the amplitude corresponds to the ionization following from the total energy of neutron absorption in the reaction $^3\mathrm{He}(n, p)T$: ~ 0.764 MeV. If a neutron is absorbed by a ^{3}He nucleus in close vicinity to an internal wall of the detector chamber, a triton or a proton (even more probable) could reach the wall; thus the ionization (and the electric signal at the electrodes) would by smaller, proportionally to the fraction of energy a triton or a proton lost in the wall. Such events provide an almost flat additional term to the differential amplitude spectrum of the electric signals measured on the detector electrodes; it ranges from the amplitude corresponding to the triton energy of 0.191 MeV to that corresponding to the total reaction energy of 0.764 MeV (Fig. 7).

If voltage applied to the detector anode is increased above ~ 1 kV, the detector will operate in the proportional regime. Free electrons from the ionization track increase their energy in the electrical field between the electrodes then transfer their energy to gas atoms in multiple collisions with them; thus drifting towards the anode with a velocity of ~ 1 cm/μs. The drifting velocity of primary ions from the ionization track is lower than that by several orders of magnitude, so they nearly do not move for the electrical signal duration, and nearly do not contribute to the signal amplitude. After drifting to the region of large electrical field strength in the vicinity of the anode, electrons will increase their kinetic energy in the electrical field between two consequent collisions with gas atoms by the amount sufficient for the gas atom ionization. Such electrons produce secondary ionization resulting in an avalanche. The avalanche increases the signal amplitude by many times; the increase factor depends on the number of generations in the avalanche. Thus the amplitude of a signal in the electrodes of the detector operated in the proportional counter regime reaches ~ 5 mV or larger; such a signal exceeds the amplitude of background signals in the detector electronics amplifier.

The gaseous UCN detector for the GRANIT spectrometer (Fig. 8) consists of a cylindrical chamber with the diameter of 4 cm and the length of 50 cm; in normal operation, the chamber axis is horizontal. The chamber is drilled in a solid duralumin block. It is covered from inside by a copper foil. A gold-coated tungsten wire with the diameter of 50 μm is stretched along the chamber axis. The wire is the anode, and the chamber is the cathode of the detector. UCN pass into the detector through a window with the height of 10 mm and the length that is nearly equal to the detector length. The window is an aluminum foil with the thickness of 0.1 mm; the vacuum tightness of the window fixation to the chamber walls is provided with a lead sealing and compression screws. Two ports are located close to two sides of the chamber, on

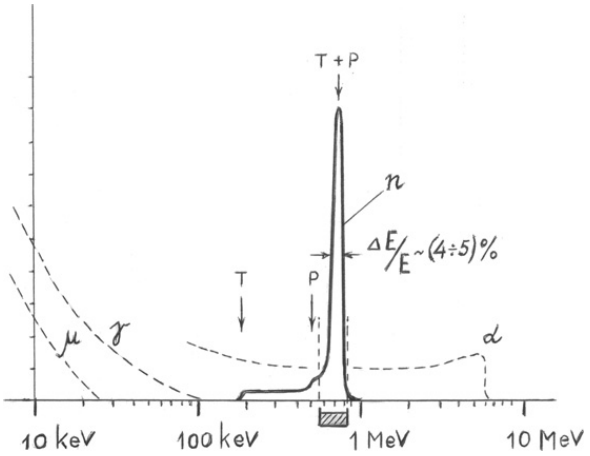

Fig. 7. A typical differential amplitude spectrum of the electrical signals at the electrodes in a UCN gaseous detector filled in with gaseous mixture containing ^{3}He; the detector is operated in the proportional counter regime. The amplitude of the electrical signal is shown on the y-axis, the ionization energy is given on the x-axis. The energies of triton (T), proton (p), and the total reaction energy ($T + p$) are indicated with arrows. Spectra of background α-particles, γ-quanta, and muons are shown with dashed lines.

Fig. 7. Un spectre typique de l'amplitude du signal électrique collecte par l'électrode d'un détecteur UCN gazeux rempli d'un mélange contenant de l'^{3}He. Le détecteur fonctionne en mode compteur proportionnel. L'amplitude du signal électrique est représentée sur l'axe y, l'énergie d'ionisation est représentée sur l'axe x. Les énergies du triton (T) du proton (p), et l'énergie de réaction totale ($T + p$) sont indiquées par des flèches. Les spectres de bruit de fond : particules α, γ et muons sont indiqués par les lignes discontinues.

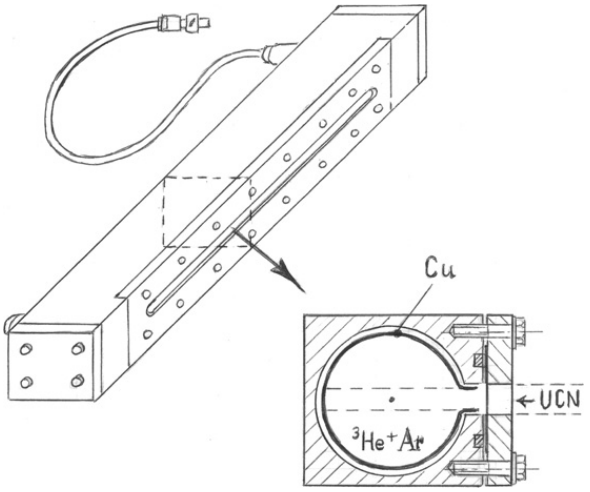

Fig. 8. A scheme of the GRANIT low-background neutron gaseous proportional counter.

Fig. 8. Schéma du détecteur de neutrons GRANIT (compteur proportionnel à faible bruit de fond).

its wall opposite to the entrance window. The first feed-through port is used for the anode wire; compressed Teflon sleeves provide its vacuum tightness. The second port is a fitting with a shut off cup; it might serve for pumping the chamber, or filling it in with gas mixture: 10 mbar of ^{3}He, 20 mbar of CO_2 and 2000 mbar of Ar. If the voltage of $\sim +1.4$ KV is applied to the anode, the detector is operated in proportional mode with the coefficient of gas amplification equal to ~ 10–20; the signal polarity is negative, its amplitude is ~ 5 mV, and the statistical scattering of signal amplitudes (FWHM for the peak $T + p \to 0.764$ MeV) is $\sim (4$–$5)\%$.

The main component of neutron background in the experimental halls in vicinity of the nuclear reactors is usually thermal neutrons; our detector is more sensitive to thermal neutrons than to neutrons of higher energy. Therefore the detector surface is protected with a cadmium foil with the thickness of 1 mm and a layer of boron rubber with the thickness of 5–6 mm; evidently, the entrance window is left unprotected. This shielding decreases background by more than an order of magnitude. The use of even thicker hydrogen and boron-containing shielding would decrease background; however, the corresponding gain factor saturates as a function of shielding thickness. Further background suppression could be achieved if the detector chamber is shielded by pure boron or by boron in some chemical composition free of hydrogen, for instance B_4C. The point is the following. The amount of boron in borated polyethylene or in boron rubber is sufficiently large for efficient absorption of thermal neutrons. However it is by far not sufficient for efficient absorption of epithermal neutrons; epithermal neutrons are originated from fast neutrons decelerated in hydrogen-containing detector shielding. These mechanisms of background generation, and protection from background, were demonstrated in the experiment [41] with a gaseous detector with the volume of ~ 40 liters (N.P.T.) of ^{3}He shielded by a layer of B_4C with the thickness of ~ 8 cm and a layer

of borated polyethylene with the thickness of ~ 30 cm placed at a distance of 7 m from the center of the active zone of the CM-2 reactor with the power of 110 MW. With proper shielding described above, we succeeded to decrease the detector background to a value corresponding to the natural α-activity of its internal walls equal to ~ 0.2 s^{-1}. Addition of small amount of borated polyethylene (where fast neutrons are slowed down to epithermal neutrons) close to the detector wall increased background by several times. Sometimes, an accelerator of protons or light nuclei in vicinity of the neutron experimental hall is the source of very fast neutrons, which are, in their turn, the dominant source of the detector background. Thus, the study in Ref. [42] showed that background in a well-shielded neutron detector placed in the experimental hall in the IBR-II reactor in Dubna was dominated by fast neutrons from the JINR synchrotron, but not from neutrons from the reactor active zone, as spectrum of accelerator neutrons is significantly harder than the spectrum of reactor neutrons. Besides, thermal or cold neutrons could be converted to very fast neutrons with the energy of 13–17 MeV via the thermonuclear reaction Li + T in Li-collimators; tritium is produced due to absorption of neutrons in ^{6}Li nuclei. Such a collimator installed in an intense beam of cold or thermal neutrons in the experimental hall is a source of fast neutrons that could be hardly shielded. Iron is most effective shielding against very fast neutrons due to the large cross section of inelastic scattering (n, n') of neutrons in iron.

Residual non-neutron background in a low-background detector results mainly from ionization in the detector caused by the natural and man-made α-activity in detector materials, by the cosmic and γ-radiation, as well as by the electronic noise, discharges and leakages in the high-voltage system of the detector. α-particles of the natural activity might be emitted from different depths in the cathode; thus the spectrum of signal amplitudes (Fig. 7) they produce extends nearly uniformly up to the energies 5–6 MeV, i.e. up to the energy of α-particles emitted from the cathode surface. A small excess of α-particle flux in vicinity of the maximum energy is due to the specific differential energy loss $(\mathrm{d}E/\mathrm{d}x)$ as a function of the α-particle energy. α-particles emitted from walls could be absorbed by a thin layer of cleaner material free of radioactive impurities. Covering of a stainless steel cathode by Teflon layer with the thickness of 60 μm in Ref. [43] decreased α-background by a factor of 10; the duralumin cathode in our GRANIT detector is covered by a copper foil with the thickness of 50 μm produced in year 1942, i.e. before the nuclear explosions in the atmosphere. α-background of our detector with a duralumin cathode was equal $(3.1 \pm 0.6) \times 10^{-3}$ s^{-1}, background decreased to $(3.9 \pm 0.8) \times 10^{-4}$ s^{-1} after covering the cathode by the copper foil; in both cases background was measured in the amplitude window of (0.67–0.85) MeV corresponding to the peak of the reaction $^3\mathrm{He}(n, p)T$.

The main component of cosmic radiation on the Earth's surface is muons with the energy $\sim 3 \times 10^{11}$ eV; their flux density is ~ 0.1 m^{-2} s^{-1}. The loss of energy of such muons in matter is 1.8 MeV/gr, i.e. they release the energy of < 20 keV in the detector gas (Ar) that is by far lower than the minimum energy of neutron detection. γ-Quanta could knock out electrons with the energy of 1 MeV and more from the detector cathode. Their ionizing power is much lower than the ionizing power of heavy charged particles (p, T, α, etc.), therefore electron paths are larger than the detector size. Thus electrons lose only a fraction of their energy in the detector, mainly to gas ionization, and produce signals with amplitudes corresponding to the absorbed energy; it is equal ~ 50 keV in our case. If the γ-quanta flux is high, signal of different γ-quanta may overlap, in particular if the momentum of the emitted electrons is nearly parallel to the detector axis and the path of electrons in the detector gas is long; then the overlapping signal amplitudes are relatively large and could reach the range of amplitudes 0.2–0.9 MeV corresponding to neutron detection. The electronic noise and electrical discharges could also contribute to this broad amplitude range, thus increasing detector background. To decrease efficiently this background, one could decrease considerably the range of detected amplitudes down to the reaction peak width, i.e. to set lower and upper thresholds of an integral discriminator so to select the peak of total absorption in the reaction $^3\mathrm{He}(n, p)T$ with the energy of 0.764 MeV. Although the efficiency of neutron detection decreases by (30–40)% in this case because of loss of events with the amplitude of neutron signal within the range of the wall effect of 0.2–0.6 MeV, nevertheless counting of events only within the peak allows in some cases to increase considerably the signal/noise ratio (7). There is a seeming temptation to decrease the wall effect due to increasing the pressure of ballast Ar, thus to increase the detector efficiency by "moving" some neutron signals from the wall effect to the peak of total absorption. This modification is particularly productive for monitor detectors, which are less sensitive then to electronics instabilities (high voltage, thresholds, amplification coefficient). However, increase of Ar pressure in UCN detectors increases also additional loss of UCN because of inelastic scattering of neutrons on Ar atoms ($\sim 6\%$ for Ar at the pressure of 1 bar), deteriorates the detector energy resolution and increases contribution of small amplitude signals originating from α- and β-activity of detector walls as well as from γ-quanta.

Background in the GRANIT UCN detector was equal $(1.2 \pm 0.2) \times 10^{-3}$ s^{-1} with the reactor on ($W = 53$ MW) and $(5.1 \pm 0.7) \times 10^{-4}$ s^{-1} with the reactor off; it was shielded by a layer of Cd with the thickness of 1 mm and a layer of borated rubber with the thickness of 6 mm, and placed to the normal position inside the GRANIT spectrometer in the level C in the ILL reactor. As UCN are produced from cold neutrons inside the cryogenic source [12] placed in close vicinity to the GRANIT spectrometer (~ 2 m) including the UCN detector, background in the UCN detector might be large. One should develop efficient shielding between the UCN source and the spectrometer, and then study feasibility of further suppression of background.

The α-background in the UCN detector could be largely suppressed by a factor of ~ 500 if one uses anticoincidence between signals of the UCN detector and signals of additional near-wall proportional counters (multi-wire system installed close to the cathode surface); the multi-wire system measures any ionizing particles coming into detector gas chamber from outside including walls [44]. In this case, background will not reach ~ 2 events per month. So low detector background

will probably never be needed for the GRANIT spectrometer; however it could be useful for some other experiments, for instance, for experimental searches for super-heavy nuclei using their spontaneous fission characterized by high multiplicity of neutron production [45], or for neutrino detector using neutron production in the interaction of a neutrino with a proton (reaction of the reverse β-decay).

5. Position-sensitive UCN detectors for measurements of gravitational levels (Alexei Muzychka)

Here we list briefly the options of applying position-sensitive detectors with a spatial resolution of the order of ~ 1 μm for measurements of gravitational quantum states in the GRANIT experiment. Nuclear track detectors with uranium coating have been used in preceding measurements [46], and described in detail in Section 2. Advantages of such detectors include high spatial resolution, simplicity of production and low cost. Disadvantages are threefold. First, these are off-line detectors, therefore one could judge on validity of every particular measurement only posteriori. Second, procedure of their chemical treatment is delicate (a detector might be destroyed or deteriorated). Third, reading out of such detectors is time-consuming: one should count many thousands of tracks using an optical microscope with extremely precision mechanical translations. That is why we would like to develop an alternative on-line position-sensitive detector.

All developments in modern real-time position-sensitive detectors for UCN of high spatial resolution have been stimulated by the present experimental program of studying gravitational quantum states of neutrons. The best spatial resolution achieved so far and high, close to 100%, efficiency of UCN detection are reported for solid-state detectors with ^{10}B and ^{6}Li convertor coatings. However, the spatial resolution in such detectors is currently limited to 5.3 μm [16,47], which is not sufficiently high to resolve spatial structures in the wave-functions of neutrons in gravitational quantum states both for a pure state, or for a mixture of states.

Therefore we consider an alternative: measuring the UCN vertical momenta distributions (instead of measuring the vertical spatial distributions) in the GRANIT experiment. In this case, a spatial resolution of position-sensitive detectors of only ~ 100 μm would be high enough. We consider a design of a position-sensitive detector for the GRANIT spectrometer, which could consist of ten Si sections connected in parallel. The detector is coated with a ^{10}B converter. The size of each section is 6 cm by 6 cm. The spatial resolution along the vertical axis is 100 μm.

6. Real-time position-sensitive detection and spectroscopy (TOF) of ultra cold neutrons with micrometric resolution (Jan Jakubek)

This section continues discussing position-sensitive UCN detectors with a spatial resolution approaching ~ 1 μm, which could be used in the GRANIT spectrometer in the future. Currently, only nuclear-track neutron detectors coated with ^{235}U, ^{10}B, or ^{6}Li [48] provide such resolution; the coordinates of UCN impact in such detectors are read out off-line in optical microscopes, often manually. An alternative on-line detector would provide significant advantages for the GRANIT spectrometer.

A perspective development concerning on-line position-sensitive UCN detectors consist of semi-conductor pixel detectors with coatings converting neutrons into heavy charged particles, which could then be detected. One such detector with a record spatial resolution of ~ 5 μm [16] is a **Timepix** detector with ^{6}Li or ^{10}B convertors.

A **Timepix** pixel device is a planar pixilated semiconductor detector, with the thickness of 300–1000 μm, bump-bonded to a Medipix readout chip, containing an amplifier, a discriminator, a counter or an ADC or a timer in each pixel cell. The pixel size in a **Timepix** detector is 55×55 μm^2; the maximum surface area of such a detector at present is 3×3 cm^2. The charged particle track coordinates are read out in such a detector using the Subpixel resolution technology. This technology is based on the fact that transport of electrons following from ionization in a semi-conductor results in electrostatic forces that repulse the electrons. Therefore the charge is collected in many pixels (~ 100); the charge values in different pixels are distributed according to the Gaussian law. The accuracy of estimating the coordinates of the maximum of measured distribution, i.e. the mean-weighted coordinates of the charged particle(s) track, could be higher than the distance between pixels by more than 2 orders of magnitude. Thus the resolution in a detector **Timepix** could reach ~ 300 nm, if a high-energy heavy charged particle arrives perpendicular to the detector plane.

The Subpixel resolution technology is based on the TOT (Time over Threshold) technology, used for fast estimation of the signal amplitude in each pixel (i.e. for measurement of the charge collected in each pixel). TOT technology uses the fact that the period, during which the signal in a pixel is higher than some threshold value, is proportional to the amplitude of this signal. In fact, the TOT technology provides a very fast amplitude analyzer of high resolution, requiring however preliminary calibration.

A mathematical model of a **Timepix** detector response to UCN was confirmed experimentally. The spatial resolution of 5.3 μm and the UCN detection efficiency of $\sim 70\%$ were achieved with a ^{6}LiF converter. A resolution of 1.5–2 μm could be estimated theoretically with a ^{10}B convertor. However, the technology of uniform thin ^{10}B coatings on such solid-sate detectors has not yet been developed well enough.

Finally, performance of a **Timepix** detector in time-of-flight mode with UCN and simultaneous measurement of UCN impact coordinates has been analyzed; relevant experimental data are presented.

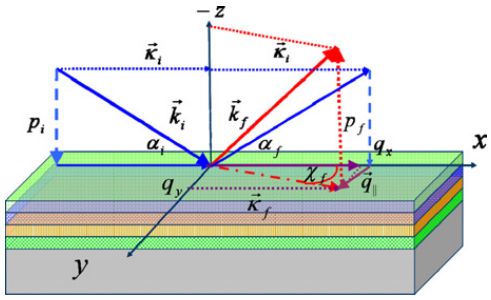

Fig. 9. Experimental kinetics.

Fig. 9. Cinématique expérimentale.

7. Introduction to elastic and inelastic neutron scattering at grazing incidence: advantages of long wavelength (Boris Toperverg)

Neutron reflectometry is nowadays a well recognized tool commonly employed to study structural organization of various thin films and multilayers (see, for instance, the recent review by Zabel et al. [49]). The main advantage of the method is that neutrons deeply penetrate into the films and, being specularly reflected from layer's interfaces, record the scattering length density (SLD) $Nb(z)$ profile across the depth of the film, or multilayer. A lateral configuration of layers is additionally accessible via resolving scattering in off-specular directions. The transverse SLD profile can routinely be retrieved from the reflection coefficient $R(q_z)$ measured as a function of the wave vector transfer component $q_z = p_f + p_i$ normal to the film surface. Here $p_i = (2\pi/\lambda_i)\sin\alpha_i$ and $p_f = (2\pi/\lambda_f)\sin\alpha_f$ are corresponding components of the incident, $\vec{k}_i$, and scattered, $\vec{k}_f$, wave vectors as indicated in the sketch of the experimental kinematics in Fig. 9.

They are experimentally controlled via an accurate definition of the incident, α_i, and reflected, α_f, glancing angles, as well as of the corresponding neutron wavelengths λ_i and λ_f, assuming that reflection process is fairly elastic. If the scattering potential $V(\vec{r},t) = V(\vec{r})$ is independent of time then scattering is elastic and $\lambda_i = \lambda_f = \lambda$, constituting one of the conditions for specular reflection. The other condition is due to the invariance of the potential against a lateral translation so that $V(\vec{r}) = V(z) = (2\pi\hbar^2/m)Nb(z)$. A combination of both conditions is resumed in the Snell's law $\alpha_i = \alpha_f$. Then, the double differential cross section of specular reflection reads [49]:

$$\left(\frac{\partial^2\sigma}{\partial\Omega\,\partial\omega}\right)_R = \frac{4S_b}{q_z^2}R(q_z)\delta(\vec{q}_\parallel)\delta(\omega) \tag{7}$$

where S_b is the cross section of the part of the primary beam illuminating the sample, $\vec{q}_\parallel = \vec{\kappa}_f - \vec{\kappa}_i$ is the lateral component of the wave vector transfer, $\hbar\omega = \hbar\varepsilon_f - \hbar\varepsilon_i$ is the energy transfer with $\hbar\varepsilon_i = \hbar^2k_i^2/2m$ and $\hbar\varepsilon_f = \hbar^2k_f^2/2m$.

The equation above is asymptotically valid in the limit $S_b \to \infty$. In practice, however, the area of the reflecting surface has to be compared with the lateral cross section of the 3D coherence ellipsoid with its principle axes $l_x \sim 1/\Delta q_x$, $l_y \sim 1/\Delta q_y$ and $l_z \sim \Delta q_z$ determined by the uncertainty principle. Hence the coherence volume is related to resolution $\Delta\vec{k}_i$ and $\Delta\vec{k}_f$ in $\vec{k}_i$ and $\vec{k}_f$, e.g. due to the angular divergence $\Delta\alpha_i$ of the incident beam, the finite angular aperture $\Delta\alpha_f$ of the detector and the wavelength spread $\Delta\lambda$. If the coherence area, i.e. the cross section of the coherence volume with the sample surface, is much smaller than the sample area, which is usually the case, then Eq. (7) should be subjected to two stage averaging. The first one assumes the averaging over the coherence range which substitutes the δ-function in Eq. (7) with the resolution function. In the second stage the result is incoherently averaged over a number of coherence areas covering the surface illuminated by the incident beam. If the surface is ideally flat and SLD is laterally homogeneous within the coherence area than only specular signal can be recorded. Alternatively, resolution limited peak of specular reflection from mean optical potential $V(z) = \langle V(\vec{r})\rangle$ is superimposed onto off-specular scattering distributed over certain range of α_f at each incident angle α_i and caused by deviations $\Delta V(\vec{r}) = V(\vec{r}) - V(z)$ of the potential from its mean value. Random deviations, e.g. those are due to interfacial roughness, lateral domains, etc. give rise to off-specular diffuse scattering, while lateral periodic structures generate off-specular Bragg peaks.

The lateral scales probed by off-specular scattering significantly depend on the particular experimental kinematics as far as the coherence ellipsoid is strongly anisotropic at low angles $\alpha_i \ll 1$, $\alpha_f \ll 1$, and $\chi_f \ll 1$. Its axis normal to the surface, i.e. the normal coherence length, l_z, may be comparable with the lateral coherence length l_y in the direction normal to the specular reflection plane. In contrast, the coherence length l_x along the intersection of the surface with the reflection plane is much greater than l_z and l_y. This is due to the fact that corresponding projection $q_x \approx (\pi/\lambda)(\alpha_i^2 - \alpha_f^2 - \chi_f^2 + \omega/\varepsilon_i)$ of the wave vector transfer is much smaller than the other two projections: $q_z \approx (2\pi/\lambda)(\alpha_i + \alpha_f)$ and $q_y \approx (2\pi/\lambda)\chi_f$ assuming $\omega/\varepsilon_i \ll 1$. As a result, with neutron wave length of 1 nm one can readily access a micrometer, or even sub-millimeter scale. This is illustrated in Fig. 10, where distribution of off-specular intensity is simulated for scattering of 10 Å neutrons from a silicon wafer patterned with the periodic array of permalloy stripes. The calculations are carried out within the framework of the Distorted Wave Born Approximation (DWBA) [49] instead of commonly applied Born Approximation

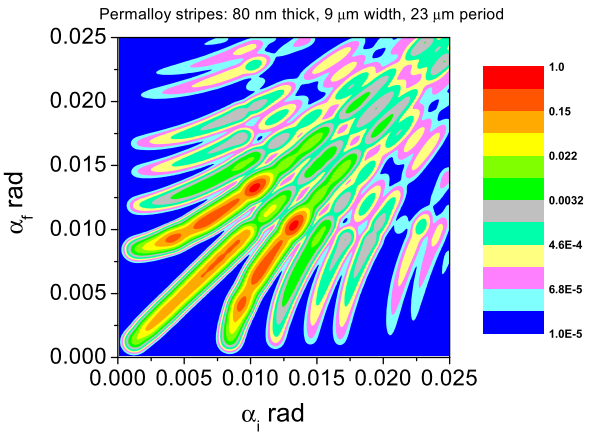

Fig. 10. Simulation of off-specular intensity.

Fig. 10. Modélisation de l'intensité non spéculaire.

(BA). The latter is, as well known, not valid if one of the wave vector components is comparable with the critical wave number q_c of the total reflection. The example mostly addressed here is scattering at grazing incidence when only one component, i.e. $q_z \sim q_c$. This example is chosen just because it well illustrate contemporary experimental situation. However, it also helps to understand the role of coherence phenomena for very cold (VCN) and ultra cold (UCN) neutrons for which all tree components of the wave vector transfer may become comparable with the critical wave vector at any incident angles. Then, BA is certainly invalid, while basic principles of DWBA may still be employed to describe interaction of VCN and UCN with laterally patterned surfaces. This is particularly the case if cold and/or very cold neutrons are sufficiently well monochromatic and collimated into the beam with the coherency remaining over a scale much greater than the neutron's wavelength. Then all features distinguished in Fig. 10 can also be identified for neutrons with substantially longer wavelengths, but impinging onto the surface under multiply increased angles, keeping, however, the incident and scattered wave numbers p_i and p_f equal to those in Fig. 10. Lets us firstly list and describe a set of the most prominent features.

The ridge in Fig. 10 running along the diagonal represents specular reflection. Its intensity distribution is calculated exactly in accordance with Eq. (1) employing the standard Parrat routine generalized for the case of polarized neutrons [49]. Rising intensity in the beginning of the ridge indicates the total reflection plateau corrected for the illumination function in Eq. (1). At higher angles one can distinguish total thickness oscillations along the specular ridge and curved side bands. The latter describe Bragg diffraction from stripes. Appreciable enhancement of off-specular scattering close to the range of the total reflection is caused by the constructive interference (Yoneda effect) between the neutron wave fields refracted to and reflected from the mean optical potential of the film. The intensity of the off-specular Bragg diffraction is calculated within the framework of the distorted wave Born approximation (DWBA) [49]. DWBA exactly takes into account distortions of incident and scattered waves in the mean optical potential, while off-specular scattering caused by $\Delta V(\vec{r})$ is regarded as perturbation.

Off-specular scattering may also be caused by inelastic scattering from excitations with absolutely flat dispersion. Such a mode can, for instance, be excited in thin films, e.g. at ferromagnetic resonance (FMR) conditions. The lateral projection of the incident wave vector in this case is conserved and $\alpha_i \neq \alpha_f$ solely due to the energy transfer $\hbar\omega \neq 0$, which violates the first ingredient of the Snell's law. If the film magnetization experiences homogeneous Larmor precession around the external field direction applied along the normal to the film surface then the magnetic part of the interaction potential $\Delta V(\vec{r}, t)$ oscillates in time with the Larmor frequency ω_L. It causes off-specular spin-flip neutron scattering with the energy transfer $\hbar\omega = \hbar\omega_L$. The scattering cross section calculated in DWBA and depicted in Fig. 11 demonstrates a sensitivity of off-specular scattering to inelasticity. As above, the strong ridge running along the main diagonal on the intensity map corresponds to specular reflection. Two side bands describe intensities of Stocks and anti-Stocks modes of off-specular scattering with the gain, and correspondingly, loss of energy. Note that inelastic scattering can be detected without any discrimination of neutrons with respect to outgoing energies. Only a moderate monochromatization (of about 1%) and collimation of the incident beam is required.

In conclusion it is worth to admit that the range off-specular scattering is dramatically enhanced for longer wavelength neutrons. In particular case of VCN and UCN it covers the total solid angle. This causes some difficulties in immediate application of UCN in a conventional reflectometry. On the other hand, neutrons with $1 < \lambda < 10$ nm have apparent perspectives to address many intriguing aspects in nano-sciences, e.g. those related to magnetic dynamics and kinetics in nano-patterns.

8. AC magnetometry with polarized neutron scattering: motivations, feasibility and applications (Kirill Zhernenkov)

AC magnetometry is a standard tool routinely applied to probe frequency dispersive properties of various magnetic materials, e.g. nano-structures employed in spintronic devices. The method is based on measurements of magnetization response to the external magnetic field $H(t)$. If the field's amplitude H_0 is small then the time-dependent part of magnetization

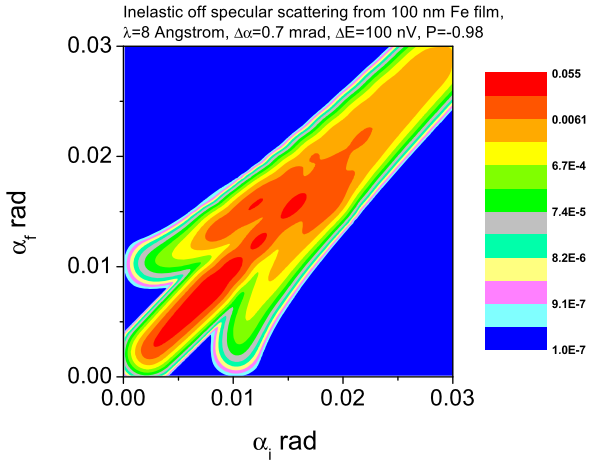

Fig. 11. Scattering cross-section calculated by DWBA.

Fig. 11. Section efficace calculée par DWBA.

can be written as $M(t) = \int \mathrm{d}t' \chi(t-t')H(t')$, where $\chi(t-t')$ is the retarded linear response function. For harmonic field $H(t) = H_0 \cos \omega_{AC} t$ the Fourier component $M(\omega_{AC}) = \chi(\omega_{AC})H_0$ is directly proportional to the homogeneous magnetic susceptibility $\chi(\omega_{AC})$, which does not provide any information about magnetization dispersion in space. On the other hand, the double differential cross section of inelastic neutron scattering is in the Born approximation (BA) proportional to the Fourier transform of the spin pair correlation function $\langle S(\vec{r},t)S(\vec{r}',t')\rangle$. The latter is related to the imaginary part of the inhomogeneous susceptibility $\chi(\vec{q},\omega)$, where $\vec{q}$ and $\hbar\omega$ are the wave vector and energy transfer. These variables are conjugated to the differences in coordinates, $\vec{\rho} = \vec{r}' - \vec{r}$, and respectively, in times, $\tau = t' - t$, assuming that the pair correlation function depends only on these differences. The latter assumption is, however, not invalid if, e.g. an AC field is applied. Then the scattered cross section depends not only on the frequency ω, but also on the time t of observation and on the AC frequency ω_{AC}. Such a dependency persists even if the scattering signal is not discriminated with respect to the energy transfer. In BA the signal is related to the instant time spin correlator, $\langle S(\vec{r},t)S(\vec{r}',t)\rangle$, and hence it is a function of t and ω_{AC}. The situation is a bit more complicated if BA is not valid, as it is the case for Polarized Neutron Reflectometry (PNR). Then, the ω_{AC}-dependent specular reflectivity is accounted for exactly, providing time and depth resolved magnetometry of thin films, multilayers, and micro- to nano-patterns. Off-specular scattering due to AC field excited lateral fluctuations can then be described in terms of the Distorted Wave Born Approximation (DWBA).

In particular, the method of AC PNR is able to provide the most complete information on the re-magnetization rate in above mentioned systems. Such information is highly required in view of current and forthcoming spintronic applications [50–52]. Since more than a decade PNR is well recognized as a tool to record the evolution of magnetization profiles under applied DC field [53,54]. Here we describe first experiments showing that AC PNR can substantially extend the capabilities of PNR by probing the magnetization distribution in space and also following its evolution in time.

The AC field device was set up as an add-on option of the ADAM reflectometer [55] at the Institute Laue–Langevin, Grenoble, France. The device (see Ref. [56] for further details) generates at the sample position an AC-field with amplitudes up to 60 Oe and frequency range 50 kHz–2 MHz. Additionally a DC-field with a maximum magnitude of 35 Oe generated by Helmholtz coils can be applied to the sample. The sample is placed inside the RF-coil together with a pick-up coil for probing and controlling the amplitude of the field at the sample position. All four reflectivities: two non-spin-flip (NSF) R^{++} and R^{--} and two spin-flip (SF), R^{+-} and R^{-+} have been measured. In addition, off-specular scattering of polarized neutrons was recorded with a position sensitive detector, but without spin discrimination of scattered neutrons. The general layout of the experimental set up and scattering kinematics are sketched in Fig. 12.

AC PNR measurements were carried out to probe the frequency and amplitude range of the AC field affecting the neutron reflectivity from two samples. The first one is a single crystalline 100 nm thick iron film. The second sample is a laterally patterned permalloy stripe array with a height 80 nm, width 9 μm, and period 3 μm. An AC magnetic field $H_{AC}(t) = H_0 \cos(2\pi f t)$ with amplitudes H_0 up to 60 Oe and frequencies $f = 300$–1800 kHz was applied along one of the easy axis (the Y-axis) within the film plane and perpendicular to the specular wave vector transfer $\vec{Q}$ normal to the surface. The additional bias field of $H_b > H_c$ was set parallel to the AC field in order to overcome the coercive field H_c and to prepare the initially magnetized state of the sample. Then a negative AC field $H_{AC} < -(H_c + H_b)$ should ensure re-magnetization of the samples in a quasi-static limit.

Fig. 13(a) shows that in an AC field of 0.3 MHz applied to Fe film the NSF reflectivities R^{++} and R^{--} are split above the angle of the total reflection. Hence, the sample magnetization averaged over the AC period $T = 3$ μs is not zero. At the same time, each of the NSF reflectivities reveals two critical edges of the total reflection. Hence the sample consists of domains with magnetization along with and opposite to the external field. Splitting between $R^{+} = R^{++} + R^{+-}$ and $R^{-} = R^{-+} + R^{--}$ is also seen in the maps of Fig. 13(b), where the specularly reflected ridge is running along the main diagonals. The splitting significantly increases with increasing frequency and reaches a maximum value above $f = 0.8$ MHz. Simultaneously off-

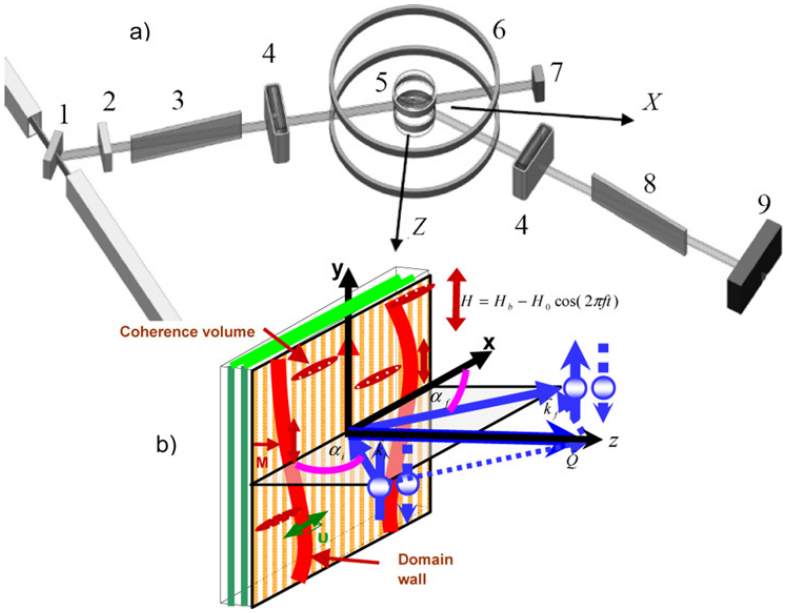

Fig. 12. Layout of the experimental set up. (a) Sketch of the ADAM neutron reflectometer (ILL, Grenoble): (1) Monochromator, (2) Be filter, (3) Polarizer, (4) Spin-flippers, (5) Sample, sample holder with radio-frequency coil, (6) Static Helmholtz coil, (7) Beam stop, (8) Analyzer, (9) Detector. (b) Scheme of the sample geometry. DC and AC fields are set collinearly with the incident polarization.

Fig. 12. Principe du dispositif expérimental. (a) Schéma du réflectomètre a neutrons ADAM (ILL, Grenoble) : (1) Monochromateur, (2) filtre Be, (3) polariseur, (4) spin-flippers, (5) échantillon et son support + bobine radiofréquence, (6) bobines de Helmholtz statiques, (7) arrêt de faisceau, (8) analyseur, (9) détecteur. (b) Géométrie de l'échantillon. Les champs continus et alternatifs sont appliqués parallèlement à la polarisation incidente.

specular scattering becomes strongly asymmetric, while finally vanishing at $f = 1.8$ MHz. The experimental observations can quantitatively be described in a scenario involving 180° Domain Wall (DW) propagation: DWs nucleated at the sample edges and/or in the bulk propagate along the X-axis against each other, erasing unfavorable domains [57]. The DW's may start to move at the time moment $t = t_0$ at which $H_{AC}(t_0) \approx -(H_c + H_b)$. If a field variation is so slow that $H_{AC}(t) \leqslant -(H_c + H_b)$ during DWs propagation till they merge together and annihilate, then reversal takes place. After reversal, the sample may stay for a certain time in a negative saturation. In an increasing field the process is reversed: DWs again nucleate and propagate back completing the re-magnetization cycle. Hence, at $H_b \neq 0$ the sample is, on average, preferentially magnetized in one direction. The fractions of the period spent in saturated and intermediate states can readily be deduced via fitting the data to the incoherent sum $R = wR(\vec{M}) + (1 - w)R(-\vec{M})$ of reflection coefficients for two magnetized states weighted with the corresponding fractions w of the period. Thus varying AC and DC field amplitudes and AC frequency one can study the re-magnetization mechanisms. In our experiments with a Fe film we carried out two sets of measurements at AC field amplitudes $H_0 = 60$ Oe and $H_0 = 55$ Oe in the presence of a bias field $H_b = 25$ Oe. From calculations it follows that for $f < 0.4$ MHz the fractions of the period well coincide with those expected from the proposed re-magnetization scenario. At elevated frequencies the negatively saturated fraction decreases and finally vanishes at $f \sim 1.5$ MHz: DWs do not succeed to pass all the way till annihilation during an AC cycle. The lowest frequency at which the magnetization reversal is no longer complete allows one to estimate the time for DW nucleation. For the present Fe sample this is on the order of 0.5 ms. So far we can only determine the re-magnetization rate of the sample, but not the DW velocity. This requires one to know the distance that the DWs travel in one cycle. Our results strongly indicate that the distance is bigger than the neutron coherence length $l_x \sim 1/(\Delta Q_x) \sim 100$ μm determined by uncertainty ΔQ_x in the lateral wave vector transfer Q_x. This gives a limit for the mean DW velocity of 30 m/s, which is much smaller than velocity ~ 1000 m/s of neutrons employed. More accurate and direct determination of the DW velocities may become available via observation of Doppler shift with use of long wavelength PNR being settled as an add-on option at GRANIT. Such PNR experiments should also shed more light on the nature on the off-specular scattering seen in Fig. 13(b), which results from magnetic inhomogeneities (DW nucleation centers, residual domains, spin waves, etc.) correlated over a distance of about 1500 nm and where magnetization directions are randomly tilted by a few degrees against the applied field. Off-specular scattering is sill detectable above the saturation field, but vanishes in static fields $H \geqslant 120$ Oe.

Dynamical correlations of magnetization in neighboring permalloy stripes were probed over the same range of fields and frequencies. In this case well structured off-specular scattering depicted in Fig. 14(b) is shaped into curved Bragg reflection bands disposed up and down with respect to the specular ridge. The effect of AC field driving DWs along stripes is seen in Fig. 14(a), where scattering intensity is plotted as a function of scattering angle α_f at fixed incident angle $\alpha_i = 10$ mrad and AC field frequencies $f = 0.5$ and 1 MHz and in the saturated state. Fig. 14(a) shows that AC field not only substantially re-distributes the scattering intensity between different orders of Bragg reflections, but also enhances diffuse scattering. This leads us to the conclusion that DWs propagate along the stripes neither simultaneously, nor randomly, but rather correlated

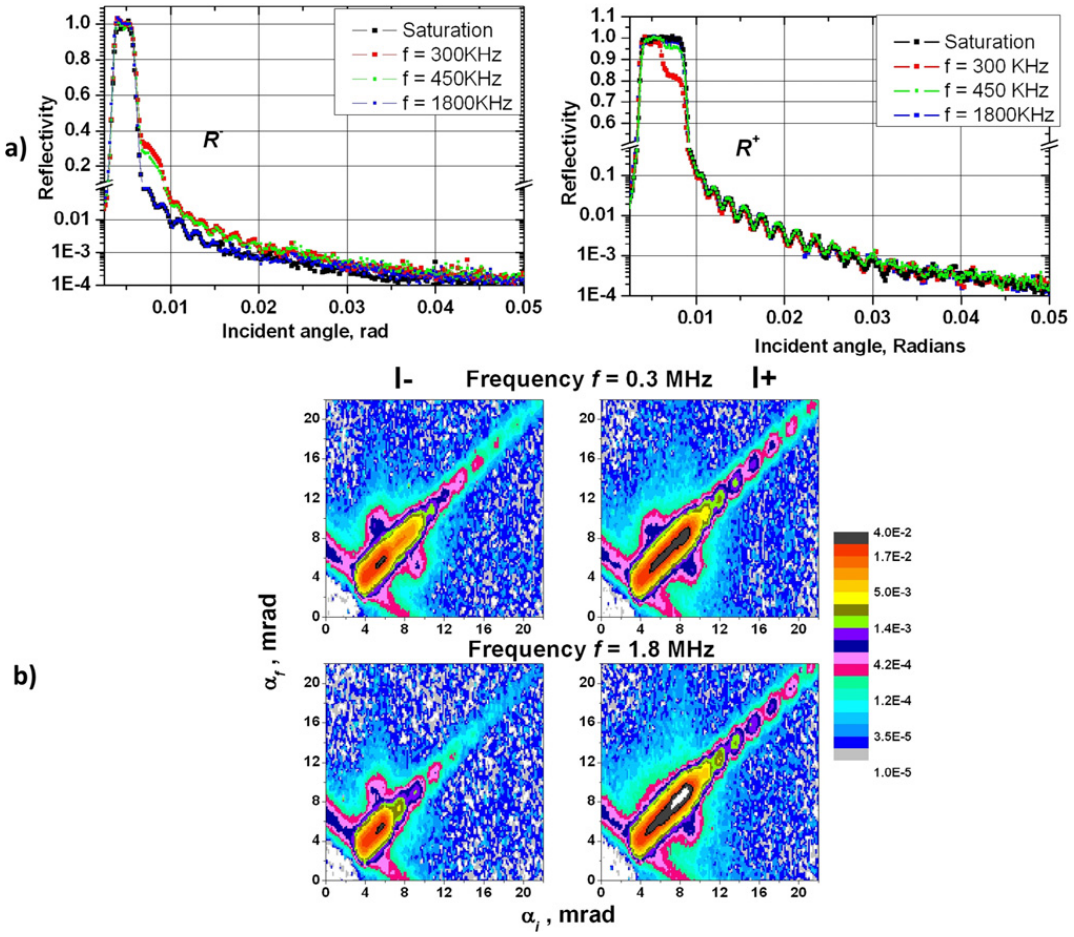

Fig. 13. a) NSF reflectivity curves R^{++} (left) and R^{--} (right) measured from Fe film in DC field $H_b = 25$ Oe set collinear with AC-field with the amplitude $H_0 = 60$ Oe at frequencies $f = 0.3$, $f = 0.45$ and $f = 1.8$ MHz. In the latter case the curves are indistinguishable from those measured in a saturating DC field $H_b = 25$ Oe with no AC field on the sample. b) Scattering maps R^- (left) and R^+ (right) recorded for 0.3 MHz (top) and 1.8 MHz (bottom). Here the AC field amplitude is $H_0 = 60$ Oe, the bias field is $H_b = 25$ Oe. Specular reflection is represented by ridges running along the lines with equal angles $\alpha_i = \alpha_f$ of incidence and scattering. The off-specular scattering seen bulging out near specular ridges is strongly asymmetric at high frequency.

Fig. 13. a) Courbes de réflectivité R^{++} (à gauche) and R^{--} (à droite) mesures pour un film de Fe en champs continu $H_b = 25$ Oe applique parallèlement au champ alternatif d'amplitude $H_0 = 60$ Oe et de fréquence $f = 0{,}3$, $f = 0{,}45$ et $f = 1{,}8$ MHz. Dans le dernier cas les courbes sont indiscernables de celles mesurées dans un champ saturant $H_b = 25$ Oe sans champ alternatif. b) Cartes de diffusion R^- (à gauche) and R^+ (à droite) enregistrées à 0,3 MHz (en haut) and 1,8 MHz (en bas). Ici l'amplitude du champ alternatif est de $H_0 = 60$ Oe, le champ de biais est de $H_b = 25$ Oe. La réflexion spéculaire est représentée par les rainures le long de la ligne $\alpha_i = \alpha_f$. La diffusion non spéculaire est fortement asymétrique à haute fréquence.

in space and time. DW nucleated in one stripe induces after a delay of DWs in a number of neighboring stripes. Further quantitative analysis of this process is in progress.

9. Collimator studies for GRANIT (Alexander Mietke)

Collimators for shaping neutron spectra for studies of gravitational quantum states and for UCN reflectometry are discussed in this section. In Ref. [12], it is predicted that the UCN source for GRANIT can provide a UCN density of $n_{\mathrm{IV}} = 800$ UCN/cm^3 in the intermediate volume, a rectangular box with the height 4 cm, the width 30 cm and the length 4 cm. The task of the collimator, which follows the intermediate volume, is to provide a collimated UCN beam with a vertical velocity which is so low that neutrons in the beam are useful to populate the lowest quantum states in the gravitational field, or eventually as a starting point for a setup for UCN reflectometry. In addition, UCN which enter the collimator, but which possess a higher vertical velocity should be reflected back into the UCN volume, so as not to reduce the UCN density in the intermediate volume. At present, the use of a "plain collimator" with a flat lower mirror and a flat, but rough upper glass plate, and a slit of 100 μm height in between, is foreseen to fulfill this task.

In this work, the same method was used as in Ref. [13], in which the plain collimator was proposed. It is assumed that UCN follow classical trajectories. From previous work on gravitationally bound quantum states (see, e.g., [8–10]), it can be concluded that for a slit height of $\Delta h = 100$ μm (or larger), the classical prediction for the transmission of the slit for UCN can be used. UCN are generated at the entrance with a uniform distribution of the starting position in the y and z coordinates, and an angular distribution, which is proportional to $\cos\theta \, \mathrm{d}\cos\theta \, \mathrm{d}\varphi$, where θ is the polar angle relative to the x-axis, and φ is the azimuthal angle. This distribution is typical for particle beams coming from a small hole in a chamber,

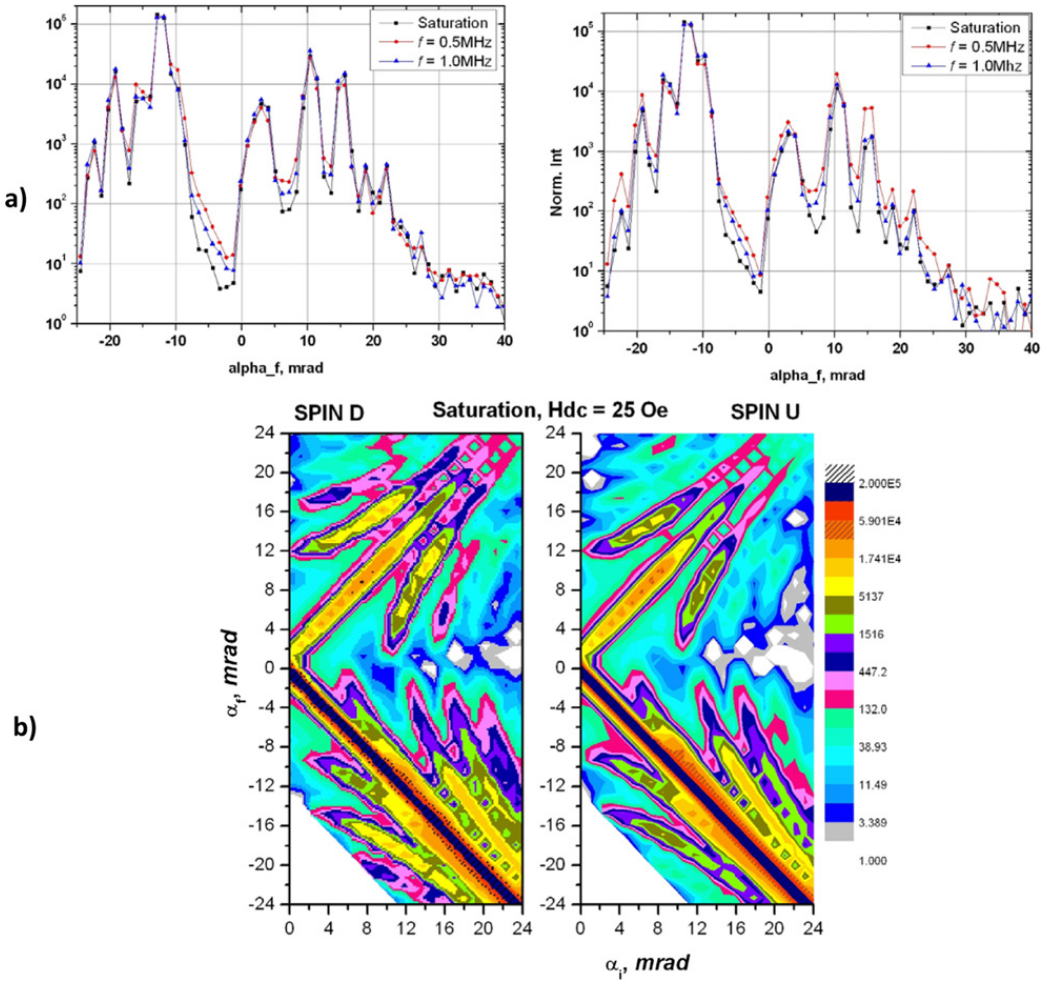

Fig. 14. a) Reflectivity cuts across $\alpha_i = 10$ mrad for R^- (left) and R^+ (right) measured in DC field $H_b = 25$ Oe set collinear with AC-field with the amplitude $H_0 = 60$ Oe at frequencies $f = 0.5$, 1.0 MHz and in the saturated state. b) Scattering maps R^- (left) and R^+ (right) recorded for saturated state of the sample in a field $H_b = 25$ Oe. Specular reflection is represented by ridges running along the lines with equal angles $\alpha_i = \alpha_f$ of incidence and scattering. The off-specular scattering is seen bulging out near specular ridges.

Fig. 14. a) Réflectivité pour $\alpha_i = 10$ mrad pour R^- (à gauche) et R^+ (à droite) mesurée dans un champ constant $H_b = 25$ Oe applique parallèlement au champ alternatif d'amplitude $H_0 = 60$ Oe et de fréquences $f = 0{,}5$, 1,0 MHz, et l'état saturé. b) Cartes de diffusion R^- (à gauche) et R^+ (à droite) enregistrées dans l'état sature de l'échantillon et un champ $H_b = 25$ Oe. La réflexion spéculaire est représentée par les rainures le long des lignes $\alpha_i = \alpha_f$. La diffusion non spéculaire se manifeste autour des rainures spéculaires.

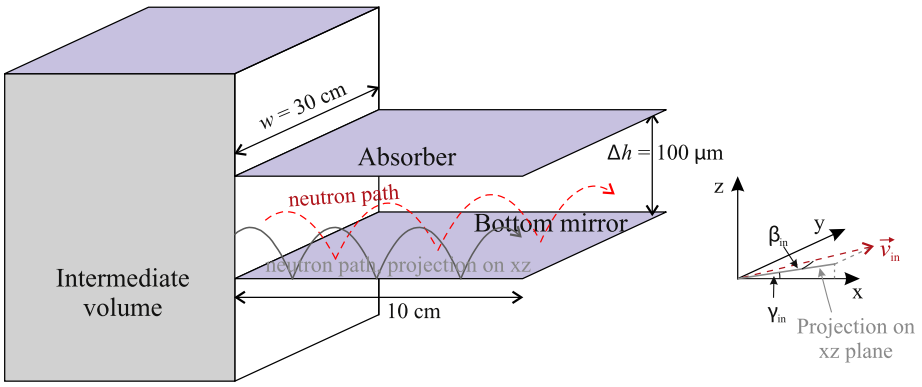

Fig. 15. Sketch of "plain" collimator, not to scale. Shown is the neutron path out of the intermediate volume through the collimator, consisting of bottom mirror and absorber (dashed line, red). We also show its projection on the xz-plane (solid line, gray). The angle γ_{in} is the angle of the incoming neutron velocity to its projection on the xz-plane. The angle β_{in} is the angle of that projection to the x-axis. (For interpretation of the references to color in this figure legend, the reader is referred to the web version of this article.)

Fig. 15. Schéma du collimateur « basique » (l'échelle n'est pas respectée). On montre le trajet des neutrons (la pointillé, rouge) depuis le volume intermédiaire à travers le collimateur qui consiste en un miroir et un absorbeur au-dessus. La projection de la trajectoire sur le plan xz est aussi représentée (la ligne solide, gris). L'angle γ_{in} est l'angle entre la vitesse incidente du neutron et sa projection sur le plan xz. L'angle β_{in} est l'angle entre cette projection et l'axe x.

in which there is a particle reservoir with uniform density and isotropic velocities. We can rewrite these conditions using the angles $\beta_{\rm in}$ and $\gamma_{\rm in}$ as defined in Fig. 15, as

$$\frac{\mathrm{d}^4 N_{\rm in}}{\mathrm{d}z_{\rm in}\,\mathrm{d}y_{\rm in}\,\mathrm{d}\beta_{\rm in}\,\mathrm{d}\gamma_{\rm in}} = \frac{1}{4\pi} n_{\rm IV} v_n \cos\gamma_{\rm in} \cos^2\beta_{\rm in} \tag{8}$$

Here, $y_{\rm in}$ and $z_{\rm in}$ are the coordinates of the point where the neutron enters the collimator, and v_n is its total velocity. We assume furthermore that the velocity distribution of UCN in the outgoing beam directly behind the slit is increasing proportional to v_n^3 between the minimum velocity of 4 m/s and maximum velocity of 7 m/s. Furthermore, we use the following rules for reflection of UCN on surfaces:

- Removal (absorption, up-scattering) of the UCN with a probability of $p_a = 3 \times 10^{-5}$.
- Diffuse reflection with the probability $p_{\rm diff}$, given by

$$p_{\rm diff} = \min\left(1 - p_{a'} \frac{r_{\rm RMS}^2 m_n^2}{h^2} v_{n,\perp}^2\right) \tag{9}$$

  Here, $r_{\rm RMS}$ is the RMS roughness of the surface, m_n is the neutron mass, h is the Planck's constant, and $v_{n,\perp}$ is the incoming UCN velocity component perpendicular to the surface.
  If a UCN undergoes diffuse reflection, its new direction is chosen such that its angular distribution, written in polar coordinates, which is proportional to $\cos\theta\,\mathrm{d}\cos\theta\,\mathrm{d}\varphi$, where θ is the polar angle relative to a normal to the surface at the reflection point.
- Otherwise: Specular reflection.
  These rules are described and adhered to in Ref. [13].

UCN, which leave the collimator exit, are called "accepted" if their classical trajectory behind the collimator is never higher than 100 μm above the lower edge of the collimator exit. In addition, we will call them "collimated" if their classical trajectory does not leave sideways a typical experimental zone that is a flat mirror of length 30 cm and width 30 cm behind the collimator. An experiment can use all accepted neutrons if its experimental zone has perpendicular side walls, and only collimated neutrons if the experimental zone has no reflecting side walls.

As a first step, we studied the plain collimator as in Ref. [13], to make contact with the previous investigations. For a plain collimator with the slit height 100 μm, the length 10 cm, the width $w = 30$ cm, and the RMS roughness of the absorber of $r_{\rm RMS} = 5$ μm, we find that 1.78% of the UCN, which enter the collimator, leave it at the exit. 0.66% of the UCN are accepted. 0.27% of the UCN are collimated. 96.54% of the UCN entering the plain collimator are reflected back into the intermediate volume, slightly more than predicted in Ref. [13]. We could trace back the small discrepancy in the last number to an error made in the implementation of the conditions described above. The remainder of the neutrons gets absorbed in the collimator.

We can calculate the rate of neutrons, which pass through the plain collimator without ever touching the top plate of the collimator. We can ignore the motion along y, and study the neutron motion projected onto the xz-plane. Neutrons, which do not touch the top plate of the collimator, fulfill the acceptance condition automatically. If a neutron moves on a simple classical trajectory, its jumping height is given by

$$z_{\rm max} = z_{\rm in} + \frac{(v_n \cos\beta_{\rm in} \sin\gamma_{\rm in})^2}{2g} \tag{10}$$

$v_n \cos\beta_{\rm in}$ is the projection of the neutron velocity on the xz-plane, and $g = 9.81$ m/s^2 is the gravitational acceleration. The classical prediction $N_{\rm out}$ of the count rate in a detector behind the absorber is that all neutrons, whose jumping height is smaller than the absorber height ($z_{\rm max} < \Delta h$), are transmitted. Then,

$$\begin{aligned}
N_{\rm out} &= \int \mathrm{d}y_{\rm in}\,\mathrm{d}\beta_{\rm in} \int\limits_{z_{\rm in},\gamma_{\rm in}\ \text{such that}\ z_{\rm max}<\Delta h} \mathrm{d}z_{\rm in}\,\mathrm{d}\gamma_{\rm in}\, \frac{\mathrm{d}^4 N_{\rm in}}{\mathrm{d}z_{\rm in}\,\mathrm{d}y_{\rm in}\,\mathrm{d}\beta_{\rm in}\,\mathrm{d}\gamma_{\rm in}} \\
&= \int_0^W \mathrm{d}y_{\rm in} \int_{-\pi/2}^{\pi/2} \mathrm{d}\beta_{\rm in} \int_{-\arcsin(\sqrt{2g(\Delta h - z_{\rm in})}/v_n\cos\beta_{\rm in})}^{\arcsin(\sqrt{2g(\Delta h - z_{\rm in})}/v_n\cos\beta_{\rm in})} \mathrm{d}\gamma_{\rm in}\, \frac{1}{4\pi} n_{\rm IV} v_n \cos\gamma_{\rm in} \cos^2\beta_{\rm in} \\
&= \int_0^W \mathrm{d}y_{\rm in} \int_{-\pi/2}^{\pi/2} \mathrm{d}\beta_{\rm in}\, \frac{\cos\beta_{\rm in}}{3\pi} \sqrt{2g\Delta h^3}\, n_{\rm IV} \\
&= \frac{2w}{3\pi} \sqrt{2g\Delta h^3}\, n_{\rm IV}
\end{aligned} \tag{11}$$

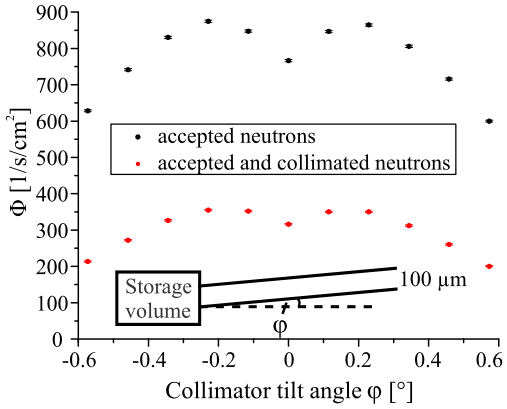

Fig. 16. Simulated neutron flux out of exit window of plain collimator for tilted collimator. The flux is calculated using $\Phi = Pn_{\mathrm{IV}}\bar{v}_n/4$, where P is the probability for a neutron entering the collimator to get to the exit. $\bar{v}_n = 5.89$ m/s is its average velocity.

Fig. 16. Flux de neutron simulé après la fenêtre de sortie du collimateur de base, pour un collimateur incliné. Le flux est calculé à partir de $\Phi = Pn_{\mathrm{IV}}\bar{v}_n/4$ ou P est la probabilité pour un neutron entrant dans le collimateur de trouver la sortie. $\bar{v}_n = 5{,}89$ m/s est la vitesse moyenne.

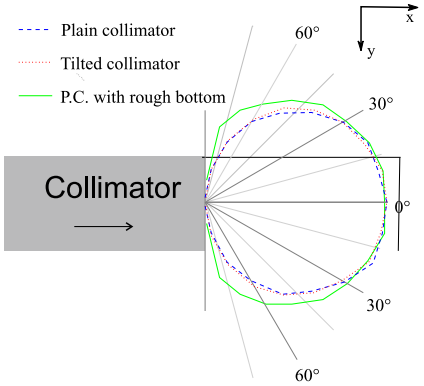

Fig. 17. Beam divergence of the outgoing accepted neutrons after the collimator for the three cases plain collimator (dashed, blue), plain tilted collimator (dotted, red) and plain collimator with rough bottom (solid, green).

Fig. 17. Divergence du faisceau de neutrons acceptés sortant du collimateur pour trois configurations : collimateur basique (tiret, bleu), collimateur basique incliné (pointillés, rouge) et collimateur basique avec un plancher rugueux (solide, vert).

We get $N_{\mathrm{out}} = 220\ \mathrm{s}^{-1}$, corresponding to an amount of neutrons passing the slit relative to the amount of neutrons entering the slit of 0.65%. The agreement with the full simulation shows that neutrons which enter the collimator in the good range of the phase space, which corresponds to a classical jumping height of less than 100 µm, go through the collimator, irrespective of the possibility of absorption in the glass. If we care about their collimation, $N_{\mathrm{collimated}} = 91\ \mathrm{s}^{-1}$ is remaining. There are two classes of neutrons, which make it through the collimator, but have too large vertical energy to be accepted. Neutrons from the first class hit the absorber several times under a small angle, and undergo specular reflections each time. The second class hits top and bottom plate many times, until they are scattered by chance into the small angular range that is allowed to get to the exit window of the collimator.

These findings show the expected improvement in UCN flux in the GRANIT setup. They compare nicely with our measured count rates in our previous setup published in Ref. [8] with roughly the same dimensions, where we detected a UCN count rate after the slit of below $1\ \mathrm{s}^{-1}$. Another observation is that it is important to have mirrors at the side of the collimator. Without them, the probability for a UCN which enters the collimator to pass through the exit side and to fulfill the acceptance condition decreases to 0.54%, and to be accepted and collimated to 0.24%. We can increase the outgoing neutron flux of good neutrons by slightly tilting the plain collimator. The reason is that with a perfectly horizontal collimator, no neutron which hit the upper glass wall while traversing the collimator can fulfill the acceptance condition. With a tilted collimator, some of these neutrons are accepted and/or collimated. The result of the simulation is shown in Fig. 16. The price to pay is a slightly wider horizontal beam divergence at the exit; on the other hand this larger divergence could become an advantage if we get side walls and prefer smaller velocity components along the neutron beam axis. The angular distribution of the neutrons exiting the collimator, as seen in top view, is shown in Fig. 17. The curve for the tilted collimator is computed for the tilt angle of 0.23°. The curves in this plot are normalized to their value at 0°. The increased horizontal divergence is in agreement with the expectation from the Liouville theorem.

An even better way to optimize the number of good neutrons coming from the plain collimator is to roughen the bottom plate. The idea is again that we can convert some of the neutrons, which bounce around in the collimator many times, into neutrons with a very low vertical energy so that they can exit the system and be accepted and/or collimated. Fig. 18 shows

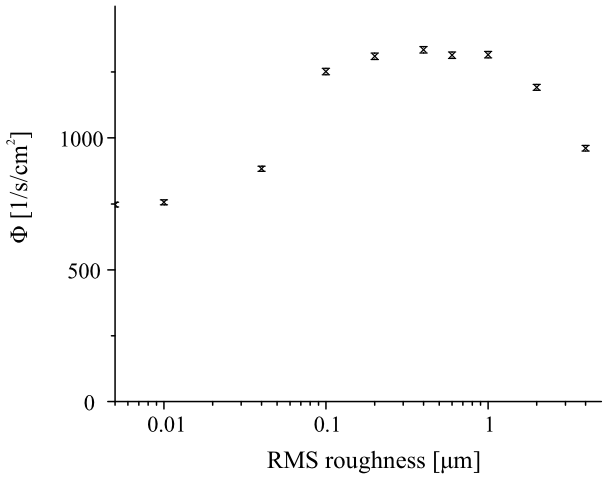

Fig. 18. Count rate of accepted neutrons as a function of bottom plate roughness.

Fig. 18. Taux de comptage des neutrons acceptés en fonction de la rugosité du miroir-plancher.

the count rate gain for different values of the roughness of the bottom plate. This gain is again at the cost of the horizontal divergence. The green curve in Fig. 17 shows the angular distribution for the outgoing neutrons for an RMS roughness of the bottom mirror of 1 μm, and, as always, 5 μm on the top mirror.

To summarize, we studied the behavior of the existing plain collimator for GRANIT, and predicted that the UCN flux for GRANIT can be improved by a factor of 1.8 with minor modifications. Further work is in preparation, in which we aim at finding a collimation system that allows selecting a desired horizontal velocity range, as it is needed for the reflectometry applications of GRANIT.

10. Reflectors for GRANIT source of UCN, and a new concept of "virtual" cold neutron source for UCN production in super-thermal helium (Egor Lychagin)

UCN for the GRANIT spectrometer will be supplied from a super-thermal helium UCN source [59], where cold neutrons are converted into UCN due to excitation of collective degrees of freedom (rotons) in super-fluid helium. In accordance to the dispersion relation for rotons, neutrons are cooled down efficiently if their wavelength equals 8.9 Å. The GRANIT UCN source is installed into a beam of neutrons with the wavelength of 8.9 Å, extracted from a neutron beam with a broad wavelength range directly looking to the cold neutron source in the ILL reactor [14].

Helium UCN sources, as well as solid-deuterium UCN sources, seem to be the most promising methods at the moment to produce UCN. There are several projects of helium UCN sources at the stage of their realization or feasibility study [14,60–63]. An advantage of helium sources is long time of UCN storage in super-fluid helium that provides accumulation of high UCN density in the source volume. A weakness of helium sources is low cross-section of UCN production (low probability of UCN production) and necessity to use very low temperatures as UCN lifetime in super-fluid He^4 depends sharply on He^4 temperature (the lifetime drops from ~ 1000 s to 30 s if the temperature increases from 0.8 to 1.2 K [64,65].

UCN density in a helium source is proportional to the average flux of cold neutrons with the wavelength of 8.9 Å also to the UCN lifetime in the source volume. The average cold neutron flux could be increased if a source is surrounded with an efficient reflector for cold neutrons. A value of the maximum gain factor in the average cold neutron flux depends on the source geometry. For the geometry of the current GRANIT UCN source, the maximum gain in cold neutron flux averaged over the source volume would reach a factor of ~ 20 for 100% efficient reflector, however, the gain factor drops sharply if the reflection efficiency decreases. An effective reflector for the existing UCN source should reflect cold neutrons elastically and the reflector thickness should be smaller than the characteristic source size to avoid diluting the cold neutron density over larger volume.

Fig. 19 shows the probability of neutron reflection from the reflectors well known in neutron physics also from a reflector made of powder of diamond nanoparticles [66] as a function of neutron velocity; the initial neutron angular distribution is isotropic. As clear from this figure, all there reflectors are not efficient for neutrons with the wavelength of 8.9 Å, except probably for a reflector made of powder of diamond nanoparticles. The results in Fig. 19 are calculated for a realistic size distribution of diamond nanoparticles; the average diamond nanoparticle diameter is ~ 3.5 nm. However, the nano-powder reflection efficiency increases when nanoparticle size decreases. Fig. 20 shows calculations of the probability of reflection of neutrons with the wavelength of 8.9 Å from a layer of hypothetical powder of diamond nanoparticles as a function of the layer thickness and the temperature; the calculations are performed within a model of independent nanoparticles with the diameter of 2 nm in rest; the powder density is 0.4 g/cm^3; the hydrogen contamination equals to values characteristic for such powders [67]; hydrogen is assumed to be rigidly attached to nanoparticle surface. As is clear from Fig. 20, the thicknesses needed to efficiently reflect neutrons are too large (compared to the existing source size) thus such reflectors would not result to any gain in the existing source geometry. Presence of hydrogen decreases the optimum

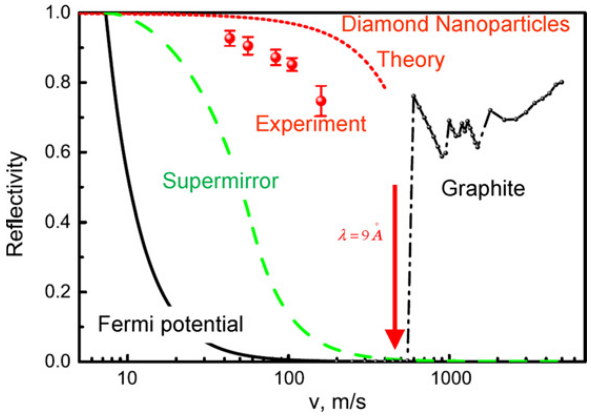

Fig. 19. The elastic reflection probability for isotropic neutron flux is shown as a function of the neutron velocity for various carbon-based reflectors: (1) Diamond-like coating (DLC) (thin solid line). (2) The best supermirror [68] (dashed line). (3) Hydrogen-free ultradiamond powder with the infinite thickness (dotted line). Calculation. (4) VCN reflection from 3 cm thick diamond nano-powder at ambient temperature (points), with significant hydrogen contamination [66]. Experiment. (5) MCNP calculation for reactor graphite reflector [69] with the infinite thickness at ambient temperature (dash-dotted line).

Fig. 19. Probabilité de réflexion pour un flux de neutrons isotrope en fonction de la vitesse des neutrons pour divers réflecteurs : (1) couches de diamant DLC (ligne fine continue), (2) le meilleur supermiroir [68] (ligne discontinue), (3) calcul pour une poudre ultradiamond sans hydrogène d'épaisseur infinie (courbe en pointillés), (4) valeur expérimentales pour la réflexion de VCN par une couche de nano-poudre de diamant d'épaisseur 3 cm a température ambiante (points) avec une contamination significative d'hydrogène [66], (5) calcul MCNP pour un réflecteur graphite de réacteur [69] pour une épaisseur infinie a température ambiante (dash-pointillé).

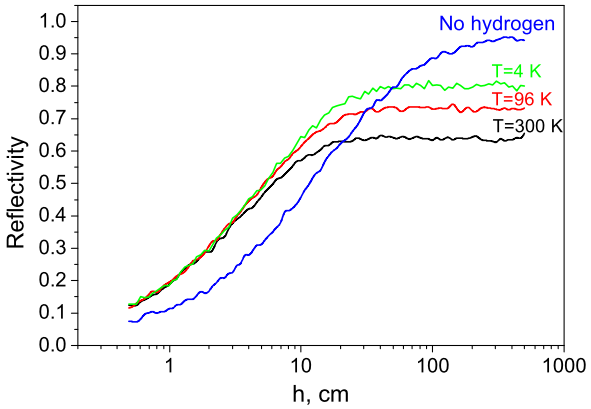

Fig. 20. The probability of reflection of neutrons with the wavelength of 8.9 Å from a hypothetical powder of diamond nanoparticles with the diameter of 2 nm; the powder density is 0.4 g/cm^3; the hydrogen contamination equals to values characteristic for such powders.

Fig. 20. Probabilité de réfection des neutrons de longueur d'onde 8,9 Å par une poudre hypothétique de nanoparticules de diamant de diamètre 2 nm, avec une densité de poudre de 0,4 g/cm^3 et une contamination en hydrogène typique pour ces poudres.

reflector thickness of equal efficiency; however it limits the best efficiency at the level of 80% (because of neutron capture in hydrogen) even if the reflector is cooled down to 4 K. It is still interesting to study other hydrogen-containing reflectors from the point of view of maximum reflection efficiency providing that the reflector thickness should not exceed a few centimeters.

We considered H_2, D_2 and methane as possible reflectors as well. Two isomeric states of H_2 orto- and para-molecules differ by the spin 0 and 1 respectively [70]. If the temperature is lower than 20 K para-state is the equilibrium one. The cross-section of elastic scattering of neutrons on para-hydrogen is small (a factor of 10 lower than that for orto-hydrogen); it is compatible with the cross-section of absorption of neutrons with the wavelength of 8.9 Å [71]. Thus the reflection probability is low because of neutron absorption and application of H_2 for neutron reflectors is not efficient. The cross-section of scattering of neutrons on orto-deuterium (equilibrium state of deuterium at low temperatures) is compatible to that on para-hydrogen [72], but it is nearly a factor of 600 larger than the absorption cross-section. So the probability of reflection of neutrons from D_2 could be high, but the reflector thickness has to be as large as about a meter.

In contrast to H_2, the probability of elastic scattering of neutrons with energies 10^{-4}–10^{-2} eV on solid methane below 20 K (in the so-called phase II) increases considerably when the temperature decreases [73]. However, the cross-section of inelastic scattering is rather large [74], so methane would not provide an efficient reflector for the current GRANIT source. Thus we have not yet found any elastic reflector for neutrons with the wavelength of 8.9 Å to be used for the GRANIT UCN source. However, the present analysis motivated us to propose a new concept of "virtual" cold neutron source at an exit of a neutron guide for producing UCN in helium.

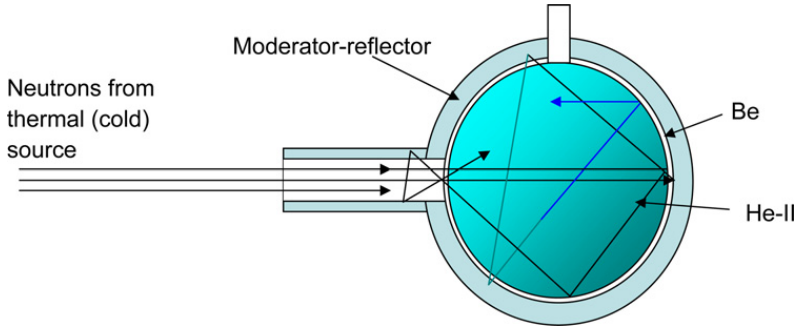

Fig. 21. Principal scheme of "external" cold neutron source for UCN super-thermal helium source.

Fig. 21. Schéma de principe d'une source « externe » de neutrons froids pour une source UCN hélium super-thermale.

A principle scheme of such a source is shown in Fig. 21. A cavity in a cryogenic cold-neutron reflector installed at the exit of a thermal (cold) neutron guide. The total flux of neutrons with the wavelength of 8.9 Å in the cavity increases compared to that in the incoming neutron guide due to multiple neutron reflection from the cavity walls as well as due to cooling the neutrons to the temperature below ~ 12 K, corresponding to the neutron wavelength of 8.9 Å. Relative γ-quanta and fast-neutron background (normalized to the total flux of useful cold neutrons) would be much lower than that present in vicinity of cold neutron sources.

As the angular divergence of neutrons in the guide is small (typically $\sim 2^\circ$ for neutron with the wavelength of 8.9 Å), cold neutrons enter the cavity of the "virtual cold neutron source" with minor scattering in the reflector entrance channel walls. If the probability of neutron reflection from the cavity walls equals unity, cold neutrons accumulate in cavity until equilibrium is reached; if so, neutron flux back to the neutron guide equals to the incoming neutron flux. One should note that the long entrance channel reflects efficiently off-axis cold neutrons back to the cavity, in analogy to phenomena considered in Refs. [13,14]. If (for the ideal reflectivity of the cavity walls) cold neutrons in the cavity would get any angle within 4π, the total cold neutron flux would become equal to that inside the reactor cold neutron source. In this case the total flux of neutrons with the wavelength of c would increase by 4 orders of magnitude (approximately the ratio of 4π-solid angle to the solid angular divergence in the incoming neutron beam) compared to that in the incoming neutron guide. We place a spherical (cylindrical) ^{4}He source in such a cavity. Storage times of UCN in the UCN accumulation volume with such shape are significantly larger than those in "guide-shape" volumes, as the storage times are proportional to the UCN mean free path. UCN transport losses are largely suppressed as experimental devices are placed close to such UCN source. There is no UCN extraction loss related to long UCN storage volumes; there is no loss related to transport of cold neutrons.

The proposed configuration of a helium UCN source provides other advantages:

- low radiation load to the cryogenic system installed to the exit of a neutron guide allows reaching the temperature of ~ 0.7 K thus long storage times of UCN in the source and consequently high UCN density in the source;
- utilization of a reflector-moderator allows us to install a helium UCN source to a thermal neutron beam; so no need for a cold neutron source in the active reactor zone.

11. Nanoparticle reflectors for cold and very cold neutrons (Egor Lychagin)

Slow neutrons, in particular Ultra Cold Neutrons (UCN, $E < 10^{-7}$ eV) and Cold Neutrons (CN, $10^{-4} < E < 10^{-2}$ eV), provide an excellent tool for various high-sensitive experiments such as searches for nonzero neutron electric dipole moment [75,76] or electric charge [77,78], precision studies of the neutron β-decay [79–81], experiments with the gravitationally bound quantum states of neutrons [7,82], and studies of fundamental symmetries [83,84]. The intermediate range of Very Cold Neutrons (VCN, $10^{-7} < E < 10^{-4}$ eV) has not been widely used in this field. However, any progress in the mentioned experiments followed always from preceding methodical developments. We studied VCN reflection from powders of diamond nanoparticles [85,86,46,87–95] and storage of VCN in closed traps with walls built of such powders. The strongly bound nanoparticles of diamond in powder provide essentially elastic reflection. VCN storage in traps might be used for constraining the neutron electric dipole moment [96] or for measuring the neutron–neutron scattering length [97]. VCN reflectors would increase considerably UCN/VCN/CN fluxes for traditional particle experiments, thus improving their sensitivity. Shaping of VCN beams using nano-structured reflectors might be used, for instance, in neutron scattering experiments constraining short-range interactions [26].

Thermal neutrons are reflected efficiently from various materials due to their diffusion motion in matter. The probability of such reflection is called albedo [98]. Large albedo value could be reached if the ratio of the neutron scattering cross-section to the absorption cross-section is high. Small penetration length of neutrons into reflector could be provided if the absolute value of the scattering cross-section is high. Among non-crystal substances, hydrogen-containing materials possess particularly large incoherent scattering cross-section, thus albedo from them could be high. However, albedo decreases for low neutron velocity v as the absorption cross section is proportional to reciprocal velocity $(1/v)$ for small values of v. Neutron albedo from crystal substances (for instance, from graphite) is high due to the coherent neutron scattering (the

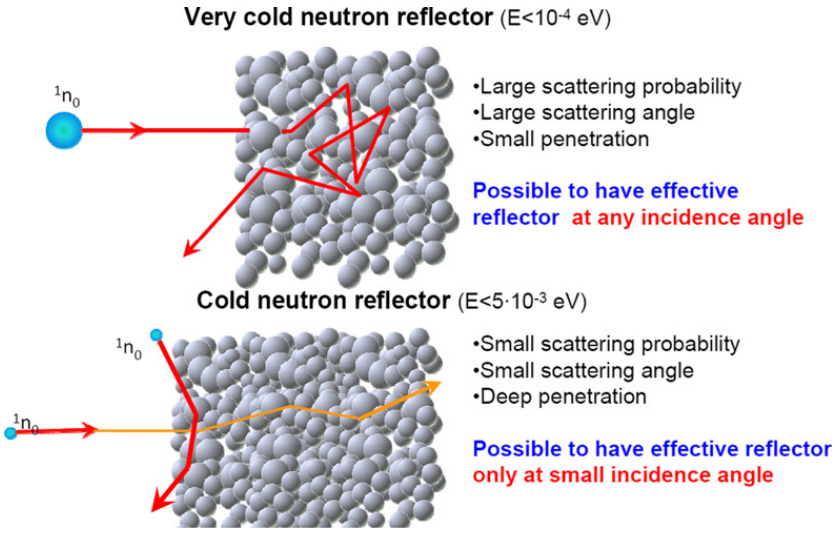

Fig. 22. Diamond nano-powder reflectors.

Fig. 22. Réflecteurs à nano-poudre de diamant.

so-called Bragg scattering [99]). Below some energy, the probability of Bragg scattering decreases sharply; the characteristic neutron wavelength corresponding to this cut-off is equal to double distance between the crystal planes. The physical reason for this cut-off consists in changing the mechanism of neutron interaction with matter: below this wavelength, neutrons interact with single nuclei; above this wavelength neutrons interact with large amount of nuclei simultaneously. As a result, the motion of neutrons with above-cutoff wavelength in matter is described in terms of effective optical potential of matter. The value of the optical potential is defined by the matter nuclear density and the amplitude of coherent scattering of nuclei in matter. If the neutron energy in vacuum is lower than the optical potential, neutron is reflected with the probability close to unity; such neutrons are called UCN. UCN could penetrate into matter to the depth of about their wavelength; they are reflected via “single bounce”, with no diffusion in matter. The maximum range of UCN energies could be effectively increased using interference effects in neutron reflection from artificial multilayer structures consisting of layers with different optical potential; such structures are called super-mirrors [100]. Using nanoparticles for reflecting very cold neutrons we return to the process of diffusion neutron motion in matter; however the characteristic scale is different and a single scattering is a more complex process. The highest efficiency of such reflection is observed if the neutron wavelength λ_n is compatible to the nanoparticle characteristic radius r ($\lambda_n \sim r$). Typical neutron albedo as a function of the neutron velocity is shown in Fig. 19 illustrating the best results for the mentioned reflection mechanisms; the initial neutron flux is isotropic.

Powders of nanoparticles could be used efficiently as first neutron reflectors covering the complete VCN energy range, thus bridging the energy gap between efficient reactor reflectors [69] for thermal and cold neutrons, and the optical potential for UCN [101]. The first experiments on the reflection of VCN from materials containing sub-micrometer structures as well as on VCN storage were carried out in the 1970s in [102] and later continued in [97]. The use of nanoparticles provides a sufficiently large cross-section for coherent scattering with the non-homogeneity of the reflector density on a spatial scale of about the neutron wave length. The large number of diffusive collisions needed to reflect VCN from powder constrains the choice of materials: only low-absorbing ones with high optical potential are appropriate. Thus, diamond nanoparticles were an evident candidate for such a VCN reflector. In order to measure precisely the VCN reflection probability from powder of diamond nanoparticles and to explore the feasibility of VCN storage in traps with nanostructured walls we carried out a dedicated experiment [66]. Measured and calculated reflectivity is shown in Fig. 19 in comparison with that for other existing neutron reflectors. The difference between theory and experimental data in Fig. 19 might be due to VCN inelastic scattering on hydrogen atoms in the powder of diamond nanoparticles. Further improvement of the VCN storage times could then be achieved by removing a part of the hydrogen from the powder in order to suppress the inelastic up-scattering of VCN. Another option consists in replacing the diamond nanoparticles by O_2, D_2, D_2O, CO_2, CO or other low-absorbing nanoparticles, free of hydrogen and other impurities with significant VCN loss cross-section.

Now, let us consider faster neutrons so that neutron wavelength $\lambda \ll r$. If so, the angle of neutron scattering on each nanoparticle is small. Therefore, neutrons arriving at a large incidence angle penetrate too deep into the powder and do not return to the surface before they are absorbed (see Fig. 22). Neutrons arriving at a small incidence angle α could return to surface after several small-angle scattering events. Such a neutron reflection is analogous to the process considered in a general form in Ref. [103], where an analytic expression describing the angular spectrum of reflected radiation is found for various laws of single scattering of ions, electrons, protons and photons from a medium consisting of scattering centers with sizes significantly larger than the radiation wavelength. As the typical number of scattering events is small, the exit angle β is not much higher than α. In addition, the penetration depth and path of neutrons in the powder are small; therefore the absorption affects reflectivity much less than that in the previous case.

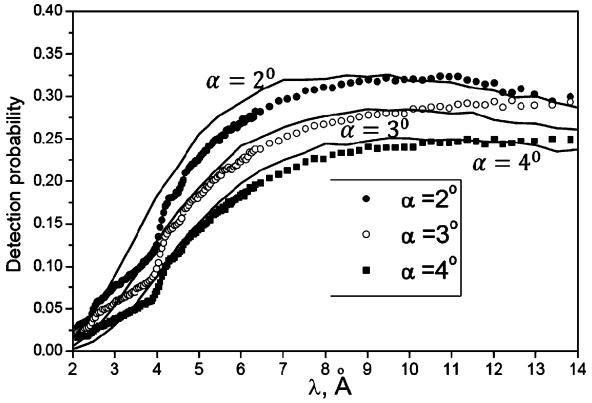

Fig. 23. The probability of neutron reflection within the detector solid angle is shown as a function of the neutron wavelength; corresponding to 40–50% total probability (albedo) of quasi-specularly scattered neutrons. The incidence angle α is equal to 2°, 3°, and 4°. Solid and empty circles as well as squares correspond to measured data; solid lines illustrate calculations.

Fig. 23. Probabilité de réfection des neutrons dans l'angle solide du détecteur en fonction de la longueur d'onde des neutrons, correspondant à une probabilité totale (albédo) de 40–50% pour la diffusion quasi-spéculaire. L'angle d'incidence α est de 2°, 3°, et 4°. Les cercles pleins, les cercles vides et les carrés correspondent aux valeurs mesurées, les lignes pleines correspondent aux calculs.

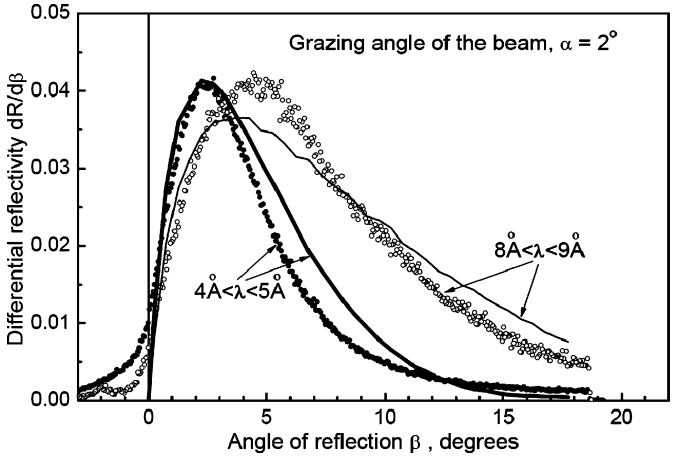

Fig. 24. Angular distributions of reflected neutrons. The incidence angle is equal 2°. Dark and empty circles correspond to measured data; solid lines illustrate calculations.

Fig. 24. Distribution angulaire des neutrons réfléchis. L'angle d'incidence est de 2°. Les cercles correspondent aux valeurs mesurées, les lignes pleines correspondent aux calculs.

In fact, for the problem parameters used in the present study, the most probable exit angle β is approximately equal to the incidence angle α, with a diffusive halo around this angle. We call such a process quasi-specular reflection. Note that coherent scattering of neutrons from neighboring nanoparticles is neglected here as it is small for the considered case $\lambda \ll r$. Besides, we neglected Mie scattering of neutrons (analogous to [29]), which assumes – in contrast to that in the first Born approximation – deviation of some neutrons to very large angles. Our simplification is justified as far as we are interested in the dominant small angle scattering. Results of a measurement [58] are shown in Figs. 23 and 24. Fig. 23 shows the probability of neutron reflection within the detector solid angle as a function of the neutron wavelength and the incidence angle. The reflectivity values in Fig. 23 are smaller than actual ones by a fraction of neutrons scattered to angles larger than the detector solid angle. Results of measurements at ambient and nitrogen temperature do not differ significantly. In particular, this is due to the small number of scattering events involved in quasi-specular reflection. Computer simulation of quasi-specular reflection is straightforward.

Fig. 24 shows measured (dark and empty circles) and calculated (solid lines) angular distributions of reflected neutrons; the neutron incidence angle is 2°. The data are averaged over two ranges of wavelengths of incident neutrons: 4–5 Å, and 8–9 Å. The neutron count rates in the position-sensitive detector for every deviation angle are divided by the incident neutron flux at the same wavelengths. Some broadening of the calculated angular distributions compared to the measured data is explained by the simplification of the model (equal sizes of nanoparticles). Nevertheless, the general agreement of the data and such a simple model are quite good. Thus, quasi-specular reflection of cold neutrons from a nano-dispersed medium occurs at small incidence angles due to several small-angle scattering of neutrons at the nano-sized inhomogeneity of the effective neutron–nuclei potential. In contrast to standard sub-critical reflection of neutrons from optical potential of uniform medium, the quasi-specular reflection might be observed also at highly above-critical angles. Moreover, powders of diamond nanoparticles used here reflect neutrons with perpendicular velocity components larger than 40 m/s, the cut-off for

the best super-mirrors available [68]. Quasi-specular reflection could find numerous applications, in particular, for neutron reflectors in zones close to a reactor core, where other reflectors would not survive radiation damage. These reflectors would increase significantly the flux of cold neutrons available for experiments.

12. Impurity quantum sols in superfluid He-II (Leonid Mezhov-Deglin)

A general idea of the equilibrium cooling of very cold neutrons to the UCN energy range in sols of weakly bound low-absorbing ultra cold nanoparticles [87] has being studied theoretically [91]. This analysis showed that such cooling is feasible provided proper choice of nanoparticles materials, nanoparticle sizes, neutron velocities, and sufficiently weak interaction between nanoparticles. Could all these conditions be provided simultaneously? A promising candidate to realize in practice all these conditions is cryogenic impurity sols of ultra cold nanoparticles in superfluid He-II; first preliminary studies of the neutron interaction with such sols are presented in Refs. [93,94].

13. Conclusion

We overviewed eventual new methodical developments for the GRANIT spectrometer and concluded that its key critical parameters could be improved further due to broader use of position-sensitive detectors, in particular real-time position-sensitive detectors, provided that background will be kept under control in analogy to previously used neutron detectors. Also we are going to develop an option of reflectometry with UCN in the GRANIT spectrometer.

Acknowledgements

The works included in this review were supported by grants, BLANC ANR-05-BLAN-0098-01 (France), NSF PHY-0855610 (USA), “Cadres” P1335-2009, P794-2010 (Russia), and RFBR 09-02-91068 (Russia).

References

[1] S. Baessler, et al., C. R. Physique 12 (2011) 707, doi:10.1016/j.crhy.2011.04.010 (in this issue).
[2] V.V. Nesvizhevsky, K.V. Protasov, J.M. Mackowski, Projet Blanc ANR-05-BLAN-0098-01, 2005–2009.
[3] M. Kreuz, et al., NIM A 611 (2009) 326.
[4] V.I. Luschikov, et al., JETP Lett. 9 (1969) 23.
[5] V.K. Ignatovich, The Physics of Ultracold Neutrons, Clarendon Press, Oxford, UK, 1990.
[6] R. Golub, D.J. Richardson, S.K. Lamoreux, Ultracold Neutrons, Higler, Bristol, 1991.
[7] V.V. Nesvizhevsky, et al., Nature 415 (2002) 297.
[8] V.V. Nesvizhevsky, et al., Phys. Rev. D 67 (2003) 102002.
[9] V.V. Nesvizhevsky, et al., Eur. Phys. J. C 40 (2005) 479.
[10] S. Baessler, Phys. G Nucl. Part. Phys. 36 (2009) 104005.
[11] V.V. Nesvizhevsky, Phys. Usp. 53 (2010) 645.
[12] Ph. Schmidt-Wellenburg, et al., NIM A 611 (2009) 267.
[13] J. Barnard, et al., NIM A 591 (2008) 431.
[14] Ph. Schmidt-Wellenburg, et al., NIM A 577 (2007) 623.
[15] V.V. Nesvizhevsky, et al., NIM A 440 (2000) 754.
[16] J. Jakubek, et al., NIM A 600 (2009) 651.
[17] V.V. Nesvizhevsky, NIM A 557 (2006) 576.
[18] V.V. Nesvizhevsky, et al., NIM A 578 (2007) 435.
[19] A.Yu. Voronin, et al., Phys. Rev. D 73 (2006) 044029.
[20] A.E. Meyerovich, et al., Phys. Rev. A 73 (2006) 063616.
[21] R. Adhikari, et al., Phys. Rev. A 75 (2007) 063613.
[22] A. Westphal, et al., Eur. Phys. J. C 51 (2007) 367.
[23] M. Escobar, et al., Phys. Rev. A 83 (2011) 033618.
[24] I. Antoniadis, et al., C. R. Physique 12 (2011) 755, doi:10.1016/j.crhy.2011.05.004 (in this issue).
[25] S. Baessler, et al., Phys. Rev. D 75 (2007) 075006.
[26] V.V. Nesvizhevsky, et al., Phys. Rev. D 77 (2008) 034020.
[27] V.V. Nesvizhevsky, A.Yu. Voronin, C. R. Physique 12 (2011) 791, doi:10.1016/j.crhy.2011.07.001 (in this issue).
[28] V.V. Nesvizhevsky, et al., Phys. Rev. A 78 (2008) 033616.
[29] V.V. Nesvizhevsky, et al., Nature Phys. 6 (2010) 114.
[30] V.V. Nesvizhevsky, et al., New J. Phys. 12 (2010) 113050.
[31] A.Yu. Voronin, et al., Phys. Rev. A 83 (2011) 032903.
[32] V.V. Nesvizhevsky, Phys. Usp. 47 (2004) 515.
[33] A. Durrani, R.K. Bull, Solid State Nuclear Track Detection. Principles, Methods and Applications, Pergamon Press, 1987.
[34] B. Doerschel, et al., NIM B 171 (2000) 423.
[35] http://www.df.unibo.it/macro/intercast/.
[36] S. Cecchini, et al., Nuovo Cimento A 109 (1996) 1119.
[37] B. Doerschel, et al., Radiation Meas. 35 (2002) 287.
[38] G. Pignol, PhD thesis, University Joseph Fourier, Grenoble, 2009.
[39] C. Krantz, Diplomarbeit, Heidelberg University, Heidelberg, 2006.
[40] E. Serge, Experimental Nuclear Physics, vol. 1, Wiley, New York–London, 1953.
[41] A.V. Strelkov, et al., Sov. Phys. JETP 47 (1978) 11.
[42] C. Kalchev, et al., JINR Reports P3-90-169, 1990.

[43] G.S. Vidiakin, et al., PTE 4 (1989) 70.
[44] K. Siegbahn (Ed.), Beta- and Gamma-Ray Spectroscopy, North-Holland, Amsterdam, 1955.
[45] G.N. Flerov, et al., Phys. At. Nucl. 20 (1974) 1.
[46] V.V. Nesvizhevsky, et al., Phys. Lett. B 479 (2000) 353.
[47] T. Sanuki, et al., NIM A 600 (2009) 657.
[48] V.V. Nesvizhevsky, et al., NIM A 440 (2000) 754.
[49] H. Zabel, K. Theis-Brohl, B.P. Toperverg, in: H. Kronmuller, S. Parkin (Eds.), Handbook of Magnetism and Advanced Magnetic Materials, vol. 1, John Willey and Sons, Chichester, 2007, p. 1.
[50] C.A. Ross, et al., Phys. Rev. B 62 (2000) 14252.
[51] P.-B. He, et al., Phys. Rev. B 72 (2005) 064410.
[52] A. Yamaguchi, et al., Phys. Rev. Lett. 92 (2004) 077205.
[53] H. Zabel, K. Theis-Brohl, B.P. Toperverg, in: H. Kronmuller, S. Parkin (Eds.), Handbook of Magnetism and Advanced Magnetic Materials, vol. 12, Wiley, New York, 2007, p. 1237.
[54] H. Zabel, et al., IEE Trans. Magn. 44 (2008) 1928.
[55] M. Wolff, et al., Thin Solid Films 515 (2007) 5712.
[56] S. Klimko, et al., Rev. Sci. Instrum. 81 (2010) 103303.
[57] K. Zhernenkov, et al., J. Phys. Cond. Mat.: Conf. Ser. 211 (2010) 012016.
[58] V.V. Nesvizhevsky, et al., Materials 3 (2010) 1768.
[59] R. Golub, et al., Phys. Lett. A 62 (1977) 337.
[60] Y. Masuda, et al., Phys. Rev. Lett. 89 (2002) 284801.
[61] G. Greene, et al., J. Res. NIST 110 (2005) 149.
[62] http://nuclear.uwinnipeg.ca/ucn/triumf/post-acot-5-26-8/ucn-post-acot-may08.pdf.
[63] A.P. Serebrov, et al., Phys. Solid State 52 (2010) 1034.
[64] R. Golub, et al., Z. Phys. B: Cond. Mat. 51 (1983) 187.
[65] Y. Abe, et al., NIM A 463 (2001) 293.
[66] E.V. Lychagin, et al., Phys. Lett. B 679 (2009) 186.
[67] V.Yu. Dolmatov, Russ. Chem. J. 70 (2001) 607.
[68] R. Maruyama, et al., Thin Solid Films 515 (2007) 5704.
[69] E. Fermi, A Course in Neutron Physics, The University of Chicago Press, Chicago, 1965.
[70] L. Farkas, Ergebn. d. exakt. Naturwiss. 12 (1933) 163.
[71] L.L. Daemen, T.O. Brun, LA-UR-98-1022.
[72] F. Atchison, et al., NIM A 611 (2009) 252.
[73] S. Grieger, et al., J. Chem. Phys. 109 (1998) 22.
[74] Y. Shin, et al., arXiv:0705.0824v2.
[75] C.A. Baker, et al., Phys. Rev. Lett. 97 (2006) 131801.
[76] I.S. Altarev, et al., Phys. Lett. B 276 (1992) 242.
[77] J. Baumann, et al., Phys. Rev. D 37 (1988) 3107.
[78] Yu.V. Borisov, et al., J. Tech. Phys. 58 (1988) 951.
[79] H. Abele, et al., Phys. Rev. Lett. 88 (2002) 211801.
[80] M. Schumann, et al., Phys. Rev. Lett. 99 (2007) 191803.
[81] S. Arzumanov, et al., Phys. Lett. B 483 (2000) 15.
[82] V.V. Nesvizhevsky, et al., Phys. Rev. D 67 (2003) 102002.
[83] V. Vesna, et al., Phys. Rev. C 77 (2008) 035501.
[84] T. Soldner, et al., Phys. Lett. B 581 (2004) 49.
[85] A.V. Strelkov, et al., NIM A 440 (2000) 695.
[86] E.V. Lychagin, et al., Phys. At. Nucl. 63 (2000) 609.
[87] V.V. Nesvizhevsky, Phys. At. Nucl. 65 (2002) 400.
[88] E.V. Lychagin, et al., Phys. At. Nucl. 65 (2002) 1995.
[89] V.V. Nesvizhevsky, Phys. Usp. 46 (2003) 93.
[90] L.P. Mezhov-Deglin, Phys. Usp. 46 (2003) 89.
[91] V.V. Nesvizhevsky, et al., Int. J. Nanoscience 6 (2007) 485.
[92] D.G. Kartashov, et al., Int. J. Nanoscience 6 (2007) 501.
[93] L.P. Mezhov-Deglin, et al., J. Low Temp. Phys. 148 (2007) 833.
[94] L.P. Mezhov-Deglin, et al., J. Low Temp. Phys. 150 (2008) 206.
[95] E.V. Lychagin, et al., Surf. Rent. Synch. Neutr. Invest. 7 (2002) 81.
[96] V.A. Artemiev, Perspekt. Mater. 7 (2008) 121.
[97] S.S. Arzumanov, et al., Phys. At. Nucl. 68 (2005) 1141.
[98] E. Amaldy, E. Fermi, Phys. Rev. 50 (1936) 899.
[99] W.L. Bragg, The diffraction of short electromagnetic waves by a crystal, Proc. Cambridge Philos. Soc. 17 (1913) 43.
[100] F. Mezei, Commun. Phys. 1 (1976) 81.
[101] V.V. Nesvizhevsky, et al., NIM A 595 (2008) 631.
[102] A. Steyerl, et al., Z. Phys. 267 (1974) 379.
[103] V.S. Remizovich, JETP 60 (1984) 290.